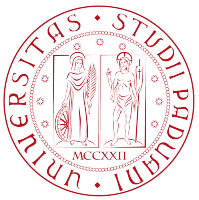

Università degli Studi di Padova

Dipartimento di Fisica e Astronomia "G. Galilei"

Corso di Laurea Magistrale in Fisica

A 3D flow focusing device for fluorescence correlation spectroscopy

Supervisor:
Prof. Sarah Köster
Georg-August-Universität Göttingen

Internal Supervisor:
Prof. Giampaolo Mistura
Università degli Studi di Padova

Co-Supervisor:
Viktor Schroeder
Georg-August-Universität Göttingen

Candidate:
Chiara Cassini

Academic Year 2014/2015

A Dino, che mi costruì un tavolo
A Tosca, che non fa che imbandirlo
A Lauretta, che mi ha impresso nei geni l'amore per i libri
A Guerrino, che mi ha insegnato a leggerli

Contents

Introduction

The first and most basic aim of physics is that of *observing* nature, in order to describe and eventually explain the profusion of different phenomenons happening around us. This observation invests all scales, from the biggest galaxy to the smallest elementary particle, and each scale needs suitable tools to be investigated properly.

More specifically, when studying living systems at cellular and sub-cellular level, a central role is played by microscopes. Microscopy is nowadays an extremely developed field, and among its current evolving branches we can find single molecule detection techniques.

The possibility of single molecule detection is offered, for instance, by fluorescence correlation spectroscopy. This microscopy method makes use of the statistical properties of molecular motion to retrieve information on the dynamics of molecules in solution, and can in principle detect one molecule at a time.

Fluorescence correlation spectroscopy also works on sample solutions in flow; small volumes of solution can stream through microchannels in a controlled fashion, as attested by the successes of microfluidics, another evolved and evolving subject.

Given the effectiveness of fluorescence correlation spectroscopy on low concentrated solutions and the growing control on small sample volumes allowed by microfluidics, a coupling of the two is most desirable.

This work intends to design and realize a microfluidic device that can serve the purpose. It shall be regarded as a preliminary approach to the problem, focused on framing the system to be built, individuating its requirements and outlining a strategy to meet such requirements; every accomplishment will be described keeping a look on possibilities of future development, in the belief that every achievement, be it humble or groundbreaking (and usually lying somewhere in between), can be perfected.

Some fundamental theoretical basis, concerning both fluorescence correlation spectroscopy and microfluidics, is established in Chapter 1. Chapter 2 deals with the design of the microfluidic device, that is actually made, and its performances experimentally evaluated, in Chapter 3.

Chapter 1

Theoretical background

In this chapter, we will have an introductory look at fluorescence correlation spectroscopy and at the advantages of coupling it with microfluidics. Fluorescence correlation spectroscopy is a microscopy technique with single molecule detection potential. Its development, based on the properties of autocorrelation functions and allowed in practice by the increasing sensibility of photon counters, started in the 1970s *[12] and has set out many other derivative detection methods (such as FCCS, ICS, N&B [6], SOFI [1], TIMMA [17]...). Very promising ways of further evolving FCS are provided by microfluidics [2, 3], another branch of physics that has turned out to be quite fruitful in the last decades. More specifically, we will concentrate on hydrodynamic flow focusing: the utility of this technique is by no means limited to the context of FCS, and this induced, in a variety of different fields, the development of many strategies to realize it.*

Section 1.1 deals with the theoretical basis of FCS, closely related to the behaviour of fluctuations in a stationary system, with the dependence of the autocorrelation function on the parameters characterizing the dynamics of the molecules examined, and with the advantages of coupling FCS with microfluidics. Section 1.2 provides a description of different flow focusing geometries, and some basic mathematical and computational instruments to treat such geometries.

1.1 Fluorescence correlation spectroscopy

1.1.1 Principles of fluorescence correlation spectroscopy

Since its first appearance at the beginning of the 20th century (following the discovery and the studies of fluorescence begun in the previous century) [15], fluorescence microscopy has been extensively developed, and it gave birth to an impressively large number of applications in optical microscopy. The success of fluorescence mainly resides in the possibility of selectively stain samples (or parts of the sample), allowing both enhanced contrast and multi-color labeling.

Among the many fluorescence microscopy techniques existing so far, fluorescence correlation spectroscopy (FCS) is particularly fit for investigating some kinetic or thermodynamic properties of diluted solutions, such as diffusion coefficients, chemical kinetic rate constants (kinetic properties), concentrations and brightnesses (thermodynamic properties) [6]. Let us consider a subvolume of a sample, more specifically the part of a solution illuminated by a laser beam. If the sample is in a stationary state, the average concentration of molecules in the subvolume is constant with time; however, as an effect of Brownian motion, particles will incessantly move in and out of the subvolume. Thus, if the molecules are fluorescent, the fluorescence from the subvolume will be subjected to random fluctuations. The autocorrelation of the detected fluorescence is related to the diffusion coefficient of the particles (as will be shown soon). Sim-

ilarly, a stationary chemical reaction during which the fluorescence changes (i.e. if fluorescent reagents give non-fluorescent products or *vice versa*) will display fluorescence fluctuations as well, because of Poissonian concentration fluctuations of the chemicals involved; these fluctuations are linked to the reaction rate constant. Before further examining the relationships between physical properties and fluctuations, let us look into the fluorescence autocorrelation function.

Given the fluorescence signal $F(t)$, detected as a function of time t and relative to a stationary process, its autocorrelation function $G(\tau)$ is defined as

$$G(\tau) = \frac{\langle \delta F(t) \delta F(t+\tau) \rangle}{\langle F(t) \rangle^2}, \tag{1.1}$$

where $\delta F(t) = F(t) - \langle F \rangle$ (the angle brackets mean averaging over time). The autocorrelation function depends on the *lag time* τ only [6]. The fluorescent signal is proportional to the number of fluorescent particles in the observed volume: the i-th fluorescent species generates from the observed volume dV a fluorescence intensity

$$dF_i(\vec{r}, t) = g_i I(\vec{r}) c_i(\vec{r}, t) dV, \tag{1.2}$$

where $\vec{r}$ is the position of the emitting molecule, t is the instant at which the emission takes place, $I(\vec{r})$ is the excitation intensity, $c_i(\vec{r}, t)$ is the concentration of the i-th species and g_i accounts for absorbance and quantum yield of the i-th species. The detector would register, for the i-th species only, a fluctuation

$$\delta F_i(t) = g_i \int I(\vec{r}) \, \mathrm{cef}(\vec{r}) \delta c_i(\vec{r}, t) dV, \tag{1.3}$$

where $\mathrm{cef}(\vec{r})$ is the collection efficiency function of the detector and the integration is taken over the volume of the entire system. From now on, it is assumed that $\mathrm{cef}(\vec{r}) = 1$ for the sake of simplicity. The actual signal is the sum of all the fluorescent species in the sample: if their number is M, then

$$F(t) = \sum_{i=1}^{M} F_i(t). \tag{1.4}$$

Similarly,

$$\delta F(t) = \sum_{i=1}^{M} \delta F_i(t), \tag{1.5}$$

so we can express the autocorrelation function as

$$\begin{aligned} G(\tau) &= \frac{\langle \sum_{i=1}^{M} \delta F_i(t) \sum_{j=1}^{M} \delta F_j(t) \rangle}{(\langle \sum_{i=1}^{M} F_i(t) \rangle)^2} = \\ &= \frac{\sum_{i=1}^{M} \sum_{j=1}^{M} g_i g_j \int I(\vec{r}) I(\vec{r'}) \langle \delta c_i(\vec{r}, 0) \delta c_j(\vec{r'}, \tau) \rangle dV dV'}{(P \sum_{i=1}^{M} g_i \langle c_i \rangle)^2} \end{aligned} \tag{1.6}$$

where $P = \int I(\vec{r}) dV$ is the laser excitation power.

From a dynamic point of view, the autocorrelation function tends to 0 when the lag time τ tends to ∞ (fluctuations very distant in time are not correlated) and the characteristic times of this decay are strictly related to macroscopic kinetic properties such as diffusion constants or reaction rate constants [18]. More specifically, the time dependence of the autocorrelation function is determined by the concentration evolution with time. Generally, the concentration fluctuations of the i-th species vary with time according to:

$$\frac{\partial \delta c_i(\vec{r}, t)}{\partial t} = D_i \nabla^2 \delta c_i(\vec{r}, t) - V_i(z) \frac{\partial c_i(\vec{r}, t)}{\partial x} + \sum T_{ij} \delta c_j(\vec{r}, t), \tag{1.7}$$

where D_i is the diffusion coefficient of the i-th species, $V_i(z)$ its convection velocity along the x-axis (perpendicular to the z-axis, which represents the excitation laser beam direction, as Figure 1.1 shows; no convection along the y-axis is assumed) and the T_{ij} coefficients account for the changes due to chemical reactions.

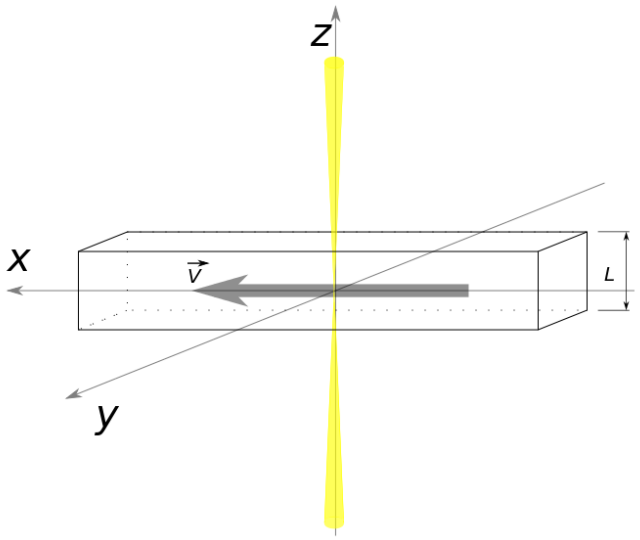

Figure 1.1: Geometry of the considered system and axis conventions.

Equation (1.7) (and thus the autocorrelation relaxation rate as well) simplifies when only one or two of these processes (diffusion, convection and chemical reaction) take place:

1. diffusion $\dfrac{\partial \delta c_i(\vec{r},t)}{\partial t} = D_i \nabla^2 \delta c_i(\vec{r},t)$;

2. convection $\dfrac{\partial \delta c_i(\vec{r},t)}{\partial t} = -V_i \dfrac{\partial c_i(\vec{r},t)}{\partial x}$;

3. chemical reaction(s) $\dfrac{\partial \delta c_i(\vec{r},t)}{\partial t} = \sum T_{ij} \delta c_j(\vec{r},t)$;

4. diffusion + convection $\dfrac{\partial \delta c_i(\vec{r},t)}{\partial t} = D_i \nabla^2 \delta c_i(\vec{r},t) - V_i \dfrac{\partial c_i(\vec{r},t)}{\partial x}$.

Anyway, in FCS the observed volume is usually defined by the illuminated volume, that is not isolated from the rest of the solution, so at least diffusion is always present (though it can become negligible when the drift velocity is high).

In a thermodynamic frame, we can ignore the time dependence of the autocorrelation and focus on its initial magnitude $G(0)$ instead. In the simple case of a single species whose brightness (i.e. photon counts per unit time due to one molecule) is q, $F(t) = qn(t)$, where $n(t)$ is the number of fluorescent molecules in the observed volume at time t, and

$$\delta F(t) = q\delta n(t) = q(n(t) - \langle n \rangle). \tag{1.8}$$

Therefore

$$G(0) = \frac{\langle(\delta F(t))^2\rangle}{\langle F\rangle^2} = \tag{1.9}$$

$$= \frac{\langle(q\delta n(t))^2\rangle}{\langle qn(t)\rangle^2} = \tag{1.10}$$

$$= \frac{\langle(\delta n(t))^2\rangle}{\langle n\rangle^2}. \tag{1.11}$$

Moreover, when the concentration is low (which is true for the typical FCS sample), the number $n(t)$ of molecules in the subvolume follows the Poissonian distribution: then $\langle(\delta n(t))^2\rangle = \langle n\rangle$, so that

$$G(0) = \langle n\rangle^{-1}. \tag{1.12}$$

This allows to compute the average number of molecules in the observed volume straightforwardly; in addiction, the brightness can be calculated too, as

$$q = \frac{\langle F\rangle}{n} = G(0)\langle F\rangle. \tag{1.13}$$

These results can be extended to take more than one species into account [6], yielding:

$$G(0) = \frac{1}{\pi w^2}\frac{\sum_{i=1}^{M}\langle c_i\rangle q_i^2}{(\sum_{i=1}^{M}\langle c_i\rangle q_i)^2}. \tag{1.14}$$

1.1.2 Dynamic influences on the autocorrelation function

Let us further examine the dependence of the autocorrelation function $G(\tau)$ on the changes in concentration. In order to do so, the solution of equation (1.7) should be substituted into (1.6). As above remarked, simplifying assumptions are recommended when handling the former, which is not analytically solvable in its most general form. In the present work, we will focus on the case where both diffusion and convection (but no chemical reaction) take place. When that is the case, each species emits independently of the others [13], so we can treat the behavior of the i-th component only, and drop the (now fixed) i subscript for the time being.

The volume of sample we need to consider is defined by the shape of the illumination light: when the source of illumination is a laser beam, we can assume a Gaussian form

$$I(\vec{r}) = I_0 \exp[-2\frac{x^2+y^2}{w^2}], \tag{1.15}$$

where I_0 is the maximum light intensity and w is the radium of the laser beam. No z dependency is present, as ensured by the low concentration of absorbing solutes [7]. w is small enough to allow to extend integrations over the ranges $-\infty \leq x \leq +\infty$ and $-\infty \leq y \leq +\infty$, while we will consider the sample extension along the z-axis, L, to be finite (see Figure 1.1). The explicit functional form for $I(\vec{r})$ provides us with another way to compute $G(0)$:

$$G(0) = \frac{g^2 \int I(\vec{r})I(\vec{r'})\langle\delta c(\vec{r},0)\delta c(\vec{r'},0)\rangle dV dV'}{(Pg\langle c\rangle)^2}. \tag{1.16}$$

Diluted solutions, which are the ones FCS microscopy deals with, can be considered ideal: then $\langle\delta c(\vec{r},0)\delta c(\vec{r'},0)\rangle = \langle c\rangle\delta(\vec{r}-\vec{r'})$ and thus

$$G(0) = \frac{\langle c\rangle \int I(\vec{r})I(\vec{r'})\delta(\vec{r}-\vec{r'})dV dV'}{(P\langle c\rangle)^2} = \frac{1}{\pi w^2 L\langle c\rangle}. \tag{1.17}$$

Note that this result is consistent with equation (1.12), because $\pi w^2 L$ is the illuminated volume.

We are now ready to investigate the form of $G(\tau)$ when only diffusion, only convection or both diffusion and convection take place.

1. **Diffusion only.** The diffusion equation

$$\frac{\partial \delta c(\vec{r},t)}{\partial t} = D\nabla^2 \delta c(\vec{r},t) \tag{1.18}$$

can be solved performing a spatial Fourier transform on $\delta c(\vec{r},t)$. Combining the information provided by this Fourier transform with equation (1.6), it can be shown [7] that

$$G(\tau) = \frac{G(0)}{1+\frac{4D}{w^2}\tau}, \tag{1.19}$$

or, defining the *characteristic diffusion time* $\tau_D \equiv \dfrac{w^2}{4D}$,

$$G(\tau) = \frac{G(0)}{1+\frac{\tau}{\tau_D}} \tag{1.20}$$

2. **Convection only.** The convective equation

$$\frac{\partial \delta c(\vec{r},t)}{\partial t} = -V(z)\frac{\partial c(\vec{r},t)}{\partial x} \tag{1.21}$$

implies that $\delta c(x,y,z,t) = \delta c(x - V(z)t, y, z, 0)$. When this is taken into account, equation (1.6) yields [13]

$$G(\tau) = \frac{G(0)}{L}\int_0^L dz e^{-\left(\frac{V(z)\tau}{w}\right)^2}. \tag{1.22}$$

The case we are mostly interested in is that of a Poiseuille flow, for which

$$V(z) = \frac{4V_m}{L^2}z(L-z) = V_m(1-\zeta^2), \tag{1.23}$$

where V_m is the maximum velocity ($V_m = V(L/2)$) and $\zeta \equiv 2/Lz - 1$. In this case, the integral is not analytically solvable, and we obtain

$$G(\tau) = G(0)\int_0^1 d\zeta e^{-(\tau/\tau_f)^2(1-\zeta^2)^2}, \tag{1.24}$$

where $\tau_f \equiv w/V_m$ is the *characteristic flow time*.

3. **Diffusion and convection.** When both diffusion and laminar flow are considered, the concentration variations are described by the equation below,

$$\frac{\partial \delta c(\vec{r},t)}{\partial t} = D\nabla^2 \delta c(\vec{r},t) - V(z)\frac{\partial c(\vec{r},t)}{\partial x}, \tag{1.25}$$

which only separates if the convection velocity is constant. Let the velocity be constantly equal to V_m first ($V(z) = V_m$). Then equation (1.25) can be solved [13], giving:

$$G(\tau) = \frac{G(0)}{1+\tau/\tau_D}\exp\left[-\frac{(\tau/\tau_f)^2}{1+\tau/\tau_D}\right]. \tag{1.26}$$

This suggests an approximate solution for the cases in which $V(z)$ is not constant, but varies slowly, that is to say if $\dfrac{\partial V(z)}{\partial z}$ is sufficiently small. Then, if additionally $w \ll L$, a good approximate solution is

$$G(\tau) = \frac{G(0)}{1+\tau/\tau_D}\int_0^1 d\zeta \exp\left[-\frac{(\tau/\tau_f)^2}{1+\tau/\tau_D}(1-\zeta^2)^2\right] \tag{1.27}$$

1.1.3 Advantages of flowing samples for fluorescence correlation spectroscopy

One of the most important applications for the FCS technique is the measurement of the degree of polymerization of fluorescence-labeled particles [6]. Such a measurement can be achieved using either the initial amplitude $G(0)$, which would provide the number of free monomers and that of polymers present in the observed volume, or analyzing the whole shape of $G(\tau)$ to compute τ_D and thus D (the latter depends on the mass of the species, allowing to discriminate between monomers, diffusing faster, and polymers, diffusing more slowly).

In any case, measurements of the entire $G(\tau)$ function is advisable [13], since the channel $\tau = 0$ is affected by shot noise and triplet kinetics, so that $G(0)$ is more precisely recovered *via* extrapolation. Hence, what we should focus on is the behaviour of the whole $G(\tau)$, described by equation (1.27) when the sample is in laminar flow.

In principle, the phenomenon we are interested in is the diffusion of the observed species, and the addition of flow complicates the functional form of $G(\tau)$ with respect to the case of simple diffusion (equation (1.20)). The advantage of a flowing sample emerges when the observed molecules diffuse slowly: in this situation, the measurement of the diffusion-only $G(\tau)$ requires long integration times, thus becoming more susceptible to system instabilities. The integration time can be reduced by setting the sample in motion: this advantage overcomes the drawback represented by the increased complexity of $G(\tau)$, which is overall modest.

In fact, the idea of coupling FCS with microchannel analytical systems finds many applications [3], thanks to the assets it implies, such as low sample consumpion and low signal to noise ratios.

Moreover, the very small volumes of sample that FCS microscopy needs can be obtained by means of hydrodynamic flow focusing, that is, enveloping the sample flow in an additional "sheath" flow used to narrow down the former. The sheath flow also prevents the sample molecules from sticking to the walls of the channel, thus reducing the risk of clogging the channel itself.

The following parts of this work will be devoted to designing, fabricating and characterizing a microfluidic device capable of flowing a low-concentration sample solution and focusing it, to be coupled with FCS detection when perfected.

1.2 Microfluidics: geometries and simulations

1.2.1 Different approaches to 3D flow focusing

Two- and three-dimensional flow focusing finds numerous applications, ranging from emulsion formation [22, 27] to microscale polymeric structures fabrication [11, 25], from rapid mixing for kinetics studies [14, 19, 24] to flow cytometry [10, 14, 23, 24, 28, 29], to single molecule detection [10, 29] and many others. Therefore, and not surprisingly, many methods have been developed to achieve the said 3D flow focusing. Flow focusing devices differ from one another mainly in their working principle and can be made of various materials, though usually the same focusing strategy can be implemented using materials of different kinds, allowing to choose the one that best suits the requirements of the experiment and the most advantageous building technique. With no pretense of being exhaustive, a list of flow focusing methods, sorted by their working principle, follows.

1. **Coaxial flow, concentric capillaries**
   Probably, the most straightforward strategy to obtain a thin stream of liquid surrounded by another liquid is that of using two concentric channels, the inner one injecting the sample solution into the outer one, in which the sheath liquid is flown.

This is the case of the first geometry described in Shah et al.'s review [22]: a cylindrical glass capillary is inserted into a square cross-sectioned one (Figure 1.2).

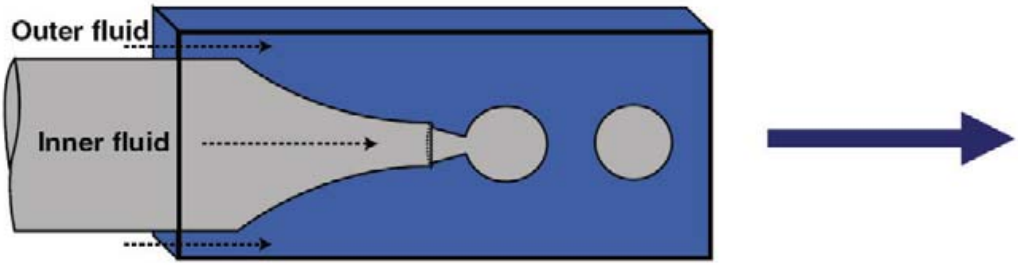

Figure 1.2: "Co-flow" geometry [22].

The inner capillary is heated and pulled using a pipette puller, in order to reduce the diameter of its tip. The coaxiality of the two capillaries is guaranteed by choosing the outer diameter of the cylindrical capillary such that it is as long as the inner diameter of the square one. If the sample solution is injected into the inner capillary and the sheath solution into the outer one, then the former will constitute a thin stream, completely surrounded by the latter and well centered into the broader capillary. This configuration (referred to as "co-flow" geometry in the review) was actually designed to create emulsions (e.g. water droplets in oil or *vice versa*); nevertheless, the narrowing down of the central stream needed for droplets formation is in fact flow focusing (streams appear in this context in the so-called "jetting regime", in which droplets form not immediately near the nozzle, but rather from the rupture of a thin jet emitted by the nozzle itself).

Similar concepts are employed by Jeong et al. [11] to build a microfluidic apparatus aimed at microscale fibers and tubes fabrication. Here, the sample stream is injected *via* a pulled

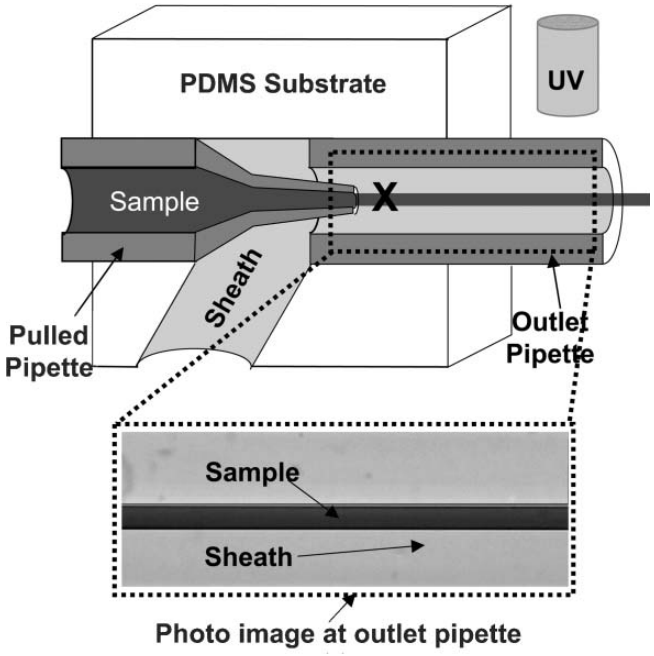

Figure 1.3: Schematic of Jeong's apparatus for fabricating microfibers [11].

pipette, too, and the outlet is a broader, non pulled pipette, but both the pipettes are inserted into a PDMS (poly(dimethylsiloxane)) substrate, which also provides an inlet for the sheath flow (Figure 1.3). All the channels involved are therefore cylindrical. The

diameter of the resulting focused stream is determined not only by the diameter of the tip of the pulled pipette, but also by the ratio between sample and sheath flow rates.

The fluid mixer described by Pabit and Hagen [19] makes again use of a circular (silica) capillary inside a square one (Figure 1.4); this time, the inner capillary is not pulled, thus it has a thin diameter all along: coaxiality is provided by a polymide coating that acts like a spacer.

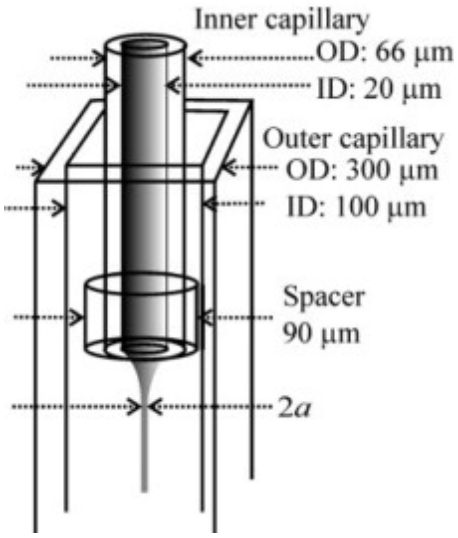

Figure 1.4: Schematic of Pabit's fluid mixer [19].

2. **Three-sides constrictions**
Multiple inlets for the sheath flow can focus the sample liquid avoiding the use of concentric capillaries. The electrical microcytomer built by Watkins et al. [28] adopts this strategy: the sample is first subjected to a two-dimensional focusing provided by symmetric injection of sheath solution from its sides; its height is then decreased as well thanks to a third sheath flow coming from the top of the channel (Figure 1.5).

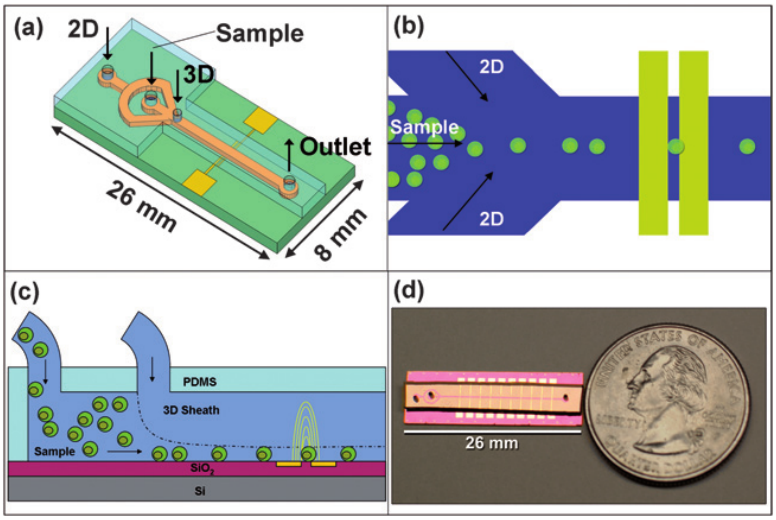

Figure 1.5: Concept of Watkin's electrical microcytometer with 3D focusing mechanism. (a) Chip-level view of the 3D hydrodynamic focusing and electrical sensing region (not drawn to scale). (b) The 2D sheaths force particles in the sample stream to flow in a single file manner and the (c) 3D sheath ensures the particles flow consistently close to the sensing electrodes. (d) Size comparison of chip to a quarter dollar [28].

All channels have three out of four walls made of PDMS (the fourth is a silicon-based substrate that hosts the electric sensors necessary for measurements). The sample is thus focused on three out of four sides: the fourth side is in contact with the sensors.

3. **Multiple layers**
   Three-dimensional focusing needs some kind of three-dimensional structure to be achieved. On the other hand, the most common fabrication techniques produce planar devices. The solution presented by Sundararajan et al. [24] is that of piling up multiple, subtle layers of planar structured PDMS. This allowed them to start from a "standard" 2D focusing design, in which a central stream is constricted from both sides by two sheath flows entering the system through lateral inlets, and to include in it additional sheath flow inlets at its top and bottom: these new streams provide the once missing vertical focusing.

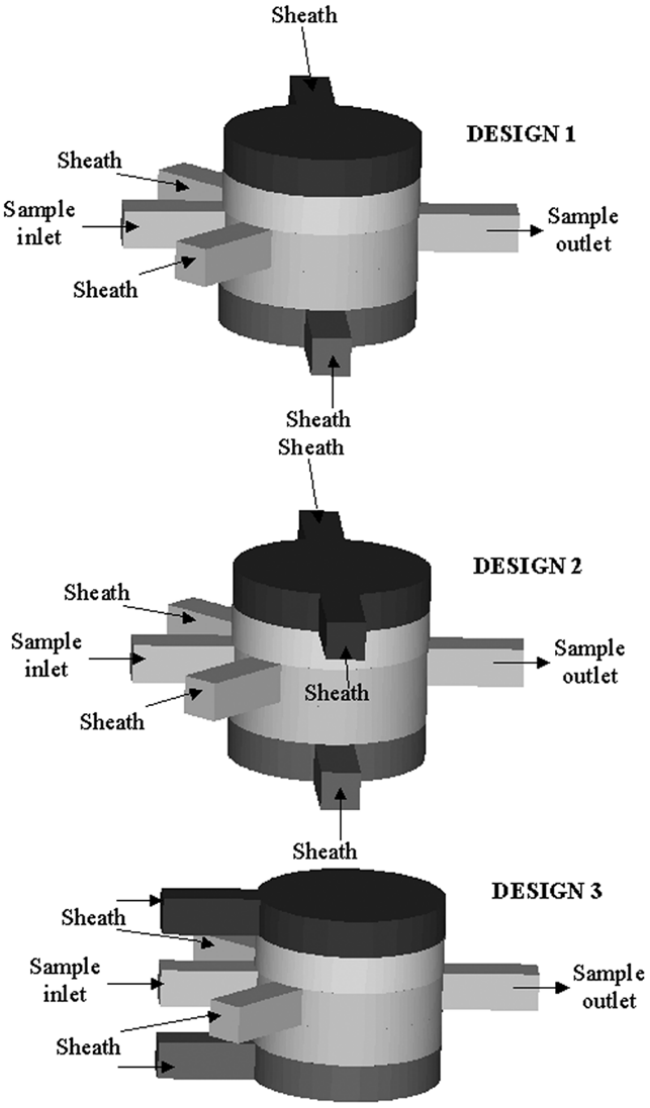

Figure 1.6: Different designs considered and simulated by Sundararajan for 3-D hydrodynamic focusing chips [24].

4. **Different heights**
   A three-dimensional structure can also be made of two layers only: that is the case of Tran et al.'s microfluidic device [27]. Both layers are made of PDMS and host channels; the channels in the upper slab have different heights. This device is used to obtain water-in-oil droplets, so the flow focusing strategy is based not only on geometry, but also on the hydrophobic or hydrophilic properties of walls and solutions.

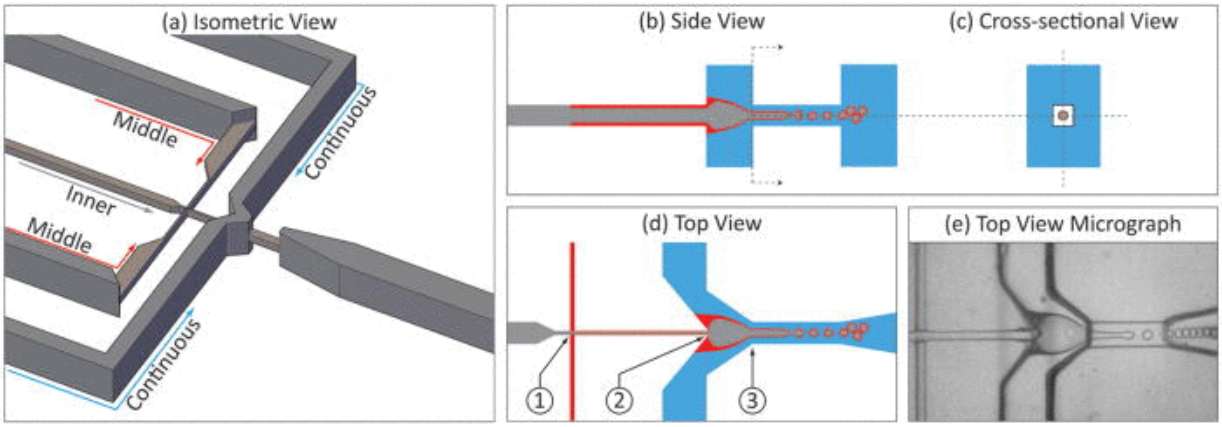

Figure 1.7: Tran's device and its working principle. (a) Isometric view of lithographically-fabricated coaxial flow focusing device, with phases labelled. (b) Side view of channels with inner (grey), middle (red), and continuous (blue) phases indicated. (c) Cross sectional view showing the square orifice enabling flow focus drop formation. (d) Schematic diagram and (e) microscope image of top view of device showing flow focus drop formation. At junction (1), the inner and middle phases combine. At junction (2), the channel expands, and the inner and middle phases combine with the continuous phase, creating the double jet. At junction (3), the double jet is focused through the orifice, generating double emulsions [27].

There are five inlets: a central one for the inner (aqueous) phase, two lateral inlets for the surrounding oil ("middle phase"), and two more lateral inlets for the "continuous" (hydrophilic) phase that constitutes the bulk of the stream (Figure 1.7). First of all, inner and middle phases are combined. The channels have all the same height, but they are hydrophobic, so that, at the cross-junction, the oil phase lifts the aqueous phase off the channels walls and surrounds it. A second junction is then reached. There, the height of the channel abruptly increases, while the aqueous (outer) phase is injected at high velocity. In this way, the oil is lifted from the walls. The three-phase jet is then focused through a small channel constriction, so that the continuous phase gains high velocity, generating high shears that rip droplets from the end of the jet.

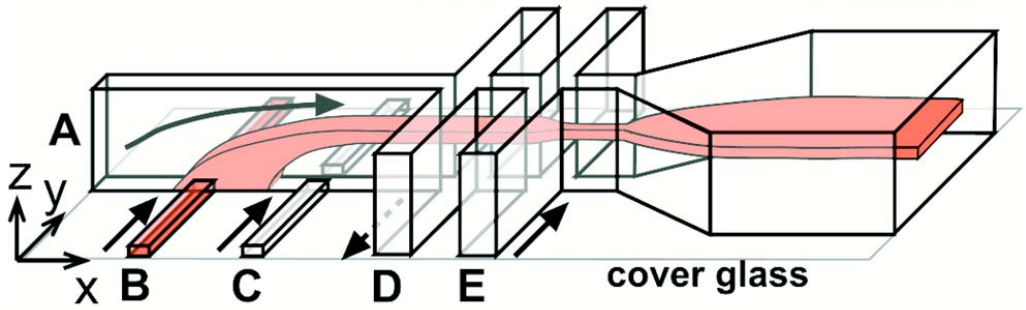

Figure 1.8: Schematic diagram showing structure of the flow in Simonnet's device with the liquid injected from port B appearing in a dark color [23].

Channels of different heights may allow three-dimensional flow focusing even if only one layer is structured, as the work of Simonnet et al. [23] points out. Here, a narrow central channel has four couples of orthogonal additional inlets (Figure 1.8). First, buffer is injected in the central channel (port A). The sample solution is injected from the first couple of lateral channels (port B): those are not only thin, but also much less tall than the central one, so they in fact inject liquids at the bottom of the central stream. The

following couple of inlets (port C) has the same size: buffer is delivered from them, so that the sample solution is lifted from the bottom, thus achieving vertical focusing. The last two couples of orthogonal channels are thicker, and as tall as the central one; the first of them (port D) is usually blocked (it was only used to test the system response to blobs), while the second (port E) provides lateral focusing.

The design just described inspired another one, that of Zhuang et al. [29], which once more makes use of channels having different heights.

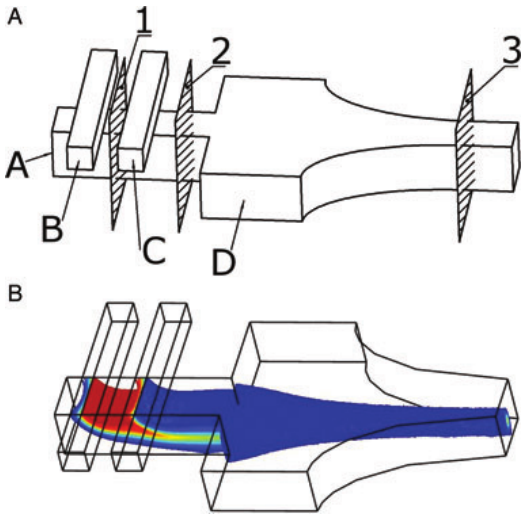

Figure 1.9: (A) Sketch showing Zhuang's two-layer structure for 3D focusing, (B) a concentration isosurface of the focused stream obtained by numerical simulation for the proposed 3D architecture [29].

The geometry is in principle very similar to that of Simmonet, though the shortest inlets, used to inject the sample and the buffer that lifts the sample from the wall, are placed at the top, instead of the bottom, of the central channel (see Figure 1.9). Moreover, the device consists once again of two structured layers: the bottom one hosts the central channel and the ones for the lateral-focusing buffer, and is made of SU-8 photoresist, while the top layer hosts the shortest inlets and is made of PDMS.

5. **Dean vortices exploitation**
   Another single-layer PDMS device capable of flow focusing was described by Mao et al. [14]. Their device exploits the formation of "Dean vortices", induced by the injection of the sample solution laterally into a sheath stream just before a 90° curve in the main channel: the centrifugal effect generates a secondary, transverse flow, made of two counter-rotating vortices located one at the top and one at the bottom of the channel (Figure 1.10). This results in a lateral drift of the sample flow, which is thus constricted in the vertical direction. Two following inlets, orthogonal to the main, and now straight, channel, provide focusing in the horizontal direction.

6. **Diagonal- and chevron-shaped grooves**
   Howell et al.'s work [10] points out how sample flows can be thinned down using microfluidic devices where diagonal or chevron-shaped grooves are present across the central channel. In the diagonal grooves design (Figure 1.11), a core and a sheath flow are introduced into a channel through the opposite ends of a T-shaped junction. The flow rate of the sheath fluid is higher than that of the sample stream, and it is injected from the inlet channel that allows it to reach the grooves first. Thanks to the diagonal grooves, the sheath flow can wrap the core fluid even on the side opposite to that of sheath inlet: the

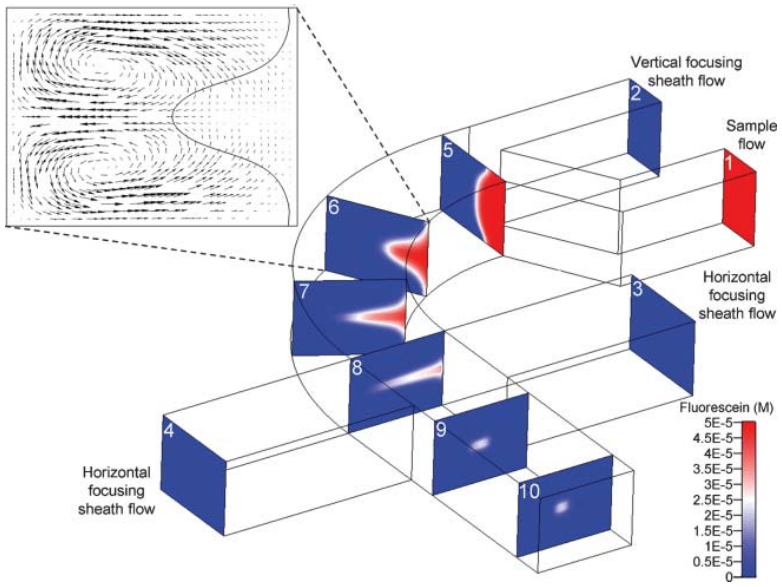

Figure 1.10: Schematic of the 3D hydrodynamic focusing process by employing the "microfluidic drifting" technique, as described by Mao [14].

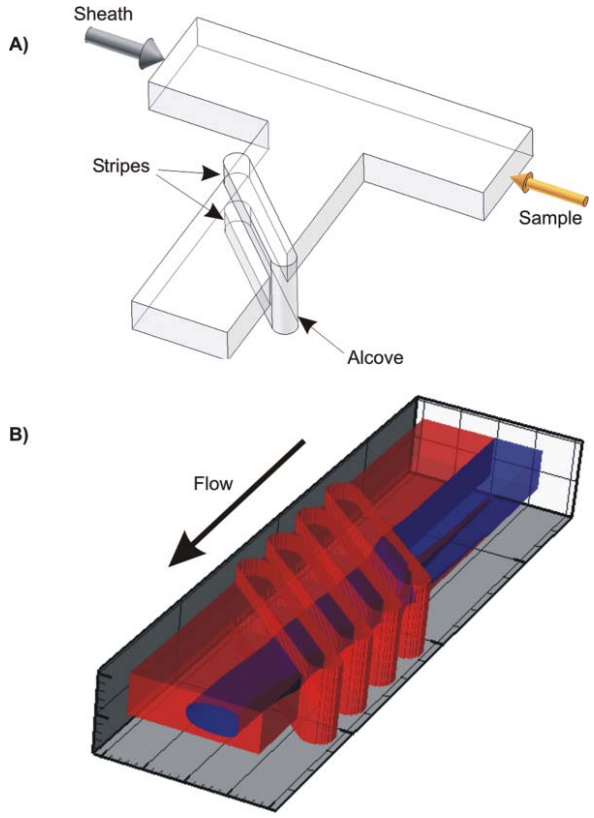

Figure 1.11: (A) Isometric schematic of Howell's stripe-based sheath flow design. (B) Computational model of the sample solution (blue) being sheathed in the sheath solution (red) [10].

wrapping is already completed after the first diagonal groove, while subsequent grooves move the sample stream further and further away from its inlet side, allowing its centering. In fact, the number of grooves controls the position of the flow, while its dimensions can be chosen varying the ratio between sheath and sample flow rates, though this influences the position too. The chevron-shaped grooves design needs an additional inlet (Figure 1.12): a central inlet is used for the sample stream, while two inlets perpendicular to the first deliver the sheath fluid. In this way, the sample fluid is always centered, as

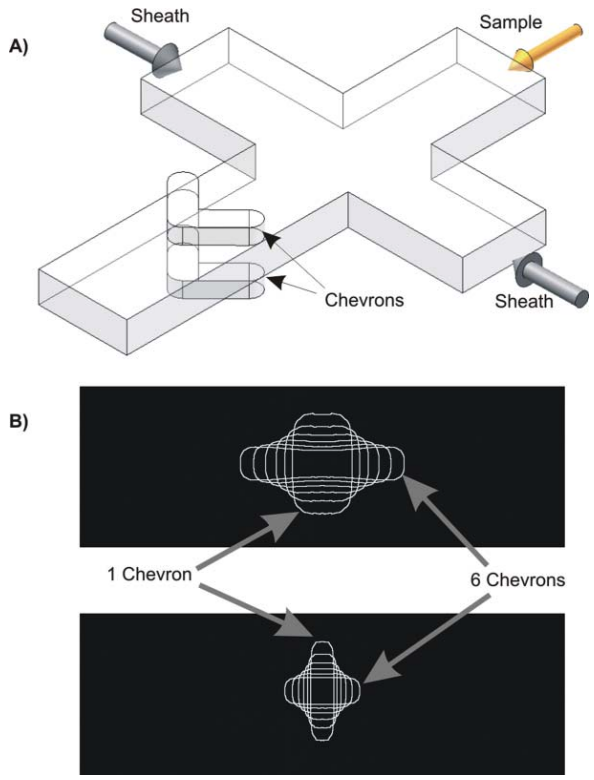

Figure 1.12: (A) Isometric schematic of Howell's chevron-based sheath flow design. The arrows indicate introduction of the respective sheath and sample solutions. (B) Shape of the sample stream modeled as a function of the number of chevron pairs [10].

long as the sheath flows are injected with equal flow rates. The height of the core stream is controlled by the number of chevrons only, while its width is related to the flow rates ratio. Thus, broad, shallow sample streams can be made as well as 3D-focused ones. These techniques where tested on devices obtained by milling, soft lithography and laser ablation, in order to demonstrate their independence of the device fabrication method.

Further development is attested by Thangawng et al.'s article [25]: chevron-shaped and diagonal grooves can be combined on the same device, using the first to choose the shape of the flow, the second to reduce its diameter.

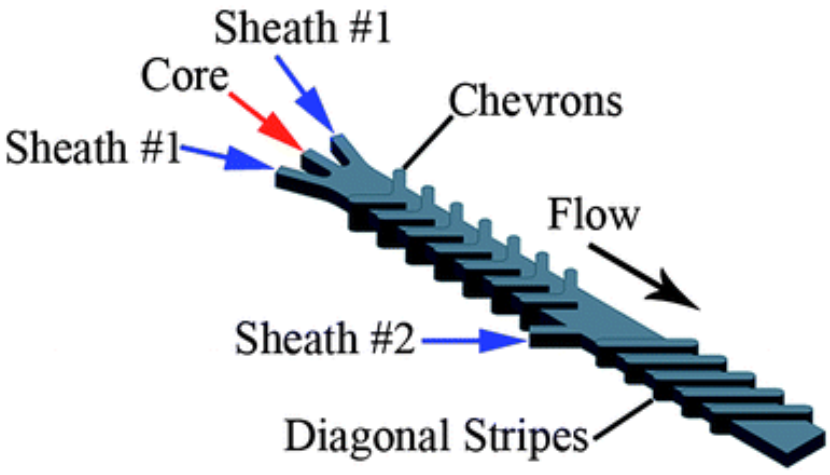

Figure 1.13: Thangawng's 7-chevron/5-diagonal groove combination design for shaping and size reduction [25].

Each of the presented flow focusing strategies have advantages and disadvantages. The use of method 1, concentric capillaries, though straightforward in principle, requires careful fabrication and handling of glass capillaries, and a good alignment is needed in order to ensure coaxiality. The mean drawback of method 2 is that it was developed to provide constrictions on only three sides of the flow, while in our case the sample stream has to be focused on all sides, and to be placed in the center of the channel, rather than flowing on its bottom. Method 3 yields a good focusing without resorting to multi-level soft lithography, but the fabrication process is long and the alignment of the layers, critical for the device to function, is quite complex. Channels of different heights, on which method 4 is based, allow the construction of smart focusing geometries that can be built in many different materials, but might need multi-level lithography, or more than one layer (and thus difficult alignment), or even both. The microfluidic drifting (i.e. method 5), on the other hand, needs neither more than one structured layer, nor different heights for the channels of a single layer, so that its fabrication is much easier; but the formation of Dean vortices, crucial for it to work, bounds the Reynolds number to be never less than 50. When using method 6, issues similar to those of method 4 arise: multi-level soft lithography is needed to provide channels with grooves (if they are made of PDMS), and the grooves have to be both on the top and on the bottom surfaces of the channel, so both halves of the device must be structured and this implies, once again, careful alignment.

1.2.2 Hydrodynamic resistance

When dealing with microfluidics, simple equations describing the examined system can be extremely useful to get fast estimates of parameters of interest such as volume flow rates or flow velocities.

In fact, the fundamental equation governing fluid dynamics, Navier-Stokes equation, is all but easy to handle in its most general form (being it a non-linear, second order partial differential equation) [9, 26]:

$$\rho\left(\frac{\partial\vec{v}}{\partial t}+(\vec{v}\cdot\vec{\nabla})\vec{v}\right)=-\vec{\nabla}p+\eta\nabla^2\vec{v}+\rho\vec{g}. \tag{1.28}$$

If, however, the studied phenomenon is stationary and in the so-called creeping flow (or Stokes flow) regime, equation (1.28) reduces to the Stokes equation [26]

$$0=-\vec{\nabla}p+\eta\nabla^2\vec{v}, \tag{1.29}$$

where, in particular, the non-linear term $(\vec{v}\cdot\vec{\nabla})\vec{v}$ is negligible. The creeping flow characterizes systems with low Reynolds numbers $Re\equiv\dfrac{\rho V_0 L_0}{\eta}$ (V_0 being the typical velocity, and L_0 the typical length scale, of the system) [26]: microfluidic systems usually belong to this category, thanks to the low velocities and lengths they involve. For example, a typical microfluidic system, of length scale $L_0\approx 100\,\mu\text{m}$, in which water ($\rho=1000\,\text{kg}\,\text{m}^{-3}, \eta=1\,\text{mPa}\,\text{s}$) flows with velocity $V_0\approx 1\,\text{mm/s}$, has a Reynolds number $Re=0.1$.

The non-linear term *exactly* vanishes when a straight channel of constant cross section is considered, because of the translational invariance of the system: this results in the Poiseuille flow, that features a parabolic velocity profile (already mentioned in Section 1.1.2, see equation (1.23)) and a constant volume flow rate Q directly proportional to the constant pressure difference Δp existing between the ends of the channel [26]. The last fact can be expressed as

$$\Delta p=R_{\text{hyd}}Q, \tag{1.30}$$

thus introducing the *hydraulic* or *hydrodynamic resistance* R_{hyd}, which only depends on the geometry of the channel and the viscosity of the liquid. This notation emphasizes the analogy existing between a fluid flow rate Q, driven by the pressure drop Δp through a channel of hydrodynamic resistance R_{hyd}, and an electric current I, driven by the electric potential drop ΔV through a resistor of electrical resistance R: for the latter another proportionality law, Ohm's law $\Delta V = RI$, is valid. Such an analogy provides the simple model we were looking for: given the geometry of a channel, we can calculate its hydrodynamic resistance and immediately have a way to estimate Q, given Δp (or the other way round).

The hydrodynamic resistance for a cylindrical channel of length l and radius r is [26]

$$R_{\text{cyl}} = \frac{8}{\pi}\eta l \frac{1}{r^4}. \tag{1.31}$$

Just like in the electrical case, the hydrodynamic resistance of a series of channels equals the sum of the resistances of the single channels. In principle, when the channels in series have different radii, the conditions for a Poiseuille flow are no longer satisfied; however, the sum rule holds for creeping flows, thanks to the absence of the non-linear term of Navier-Stokes equation. The hydrodynamic resistance of a trunk cone of length l and base radii r_1 and r_2 ($r_1 > r_2$) may then be calculated as a series of cylindrical channels of infinitesimal length dx:

$$R_{\text{cone}} = \int dR = \int_0^l \frac{8}{\pi}\eta dx \frac{1}{[r(x)]^4}. \tag{1.32}$$

Expressing $r(x)$ as $r(x) = r_1 - \dfrac{r_1 - r_2}{l}x$, it follows that

$$R_{\text{cone}} = \frac{8}{3\pi}\eta \frac{l}{r_1 - r_2}\left(\frac{1}{r_2^3} - \frac{1}{r_1^3}\right). \tag{1.33}$$

These expressions will help us characterizing the systems studied in the experimental section.

1.2.3 Finite element method simulations

A detailed description of more complex microfluidic geometries requires computational fluid dynamics (CFD). CFD is used to predict the behaviour of fluids, given the geometrical and physical environment they are in [9]. The mathematical expressions that describe the system dynamics (usually partial differential equations) often prove to be difficult (or impossible) to solve analytically: approximate solutions can be numerically computed, if the equations are suitably discretized.

A CFD method especially useful when handling complex geometries [9] is the finite element method (FEM). Briefly, FEM consists in dividing the considered geometric domain in subdomains ("finite elements") and computing a different solution for each; these solutions have to be continuous on their own subdomain, and continuity is also required when passing from one element to another [8, 26].

All FEM simulations of this work are performed using COMSOL Multiphysics® 5.0 and its CFD Module. COMSOL is a commercial software that manages the computational problem step-by-step, from the definition of the geometry to that of the species involved, from the boundary conditions, to the meshing, to the actual computation.

As an example, suppose we want to verify equation 1.33: we can simulate the motion of water into a trunk cone-shaped pipe, induced by a pressure difference of our choice, in creeping motion regime, and see how the volume flow rate through the channel varies with said pressure difference. We expect a plot of flow rates against pressure distances to be linear, with the angular coefficient of the interpolating line equal to $1/R_{\text{cone}}$. This value of R_{cone} can then be

compared with the same quantity calculated through equation 1.33 from the geometry of the system. We will then consider a trunk cone of length $l = 1\,\text{mm}$ and base radii $r_1 = 50\,\mu\text{m}$ and $r_2 = 5\,\mu\text{m}$. When water (viscosity $\eta = 1\,\text{mPa}\,\text{s}$) flows inside it, the hydrodynamic resistance opposed by the channel, according to equation 1.33, is $R_{\text{cone}} = 1.5 \cdot 10^{14}\,\text{Pa}\,\text{s}\,\text{m}^{-3}$. This is transposed into a COMSOL simulation through the following steps:

Geometry definition. The geometry just described can be easily entered stating the values for l, r_1, $r2$. This results in Figure 1.14.

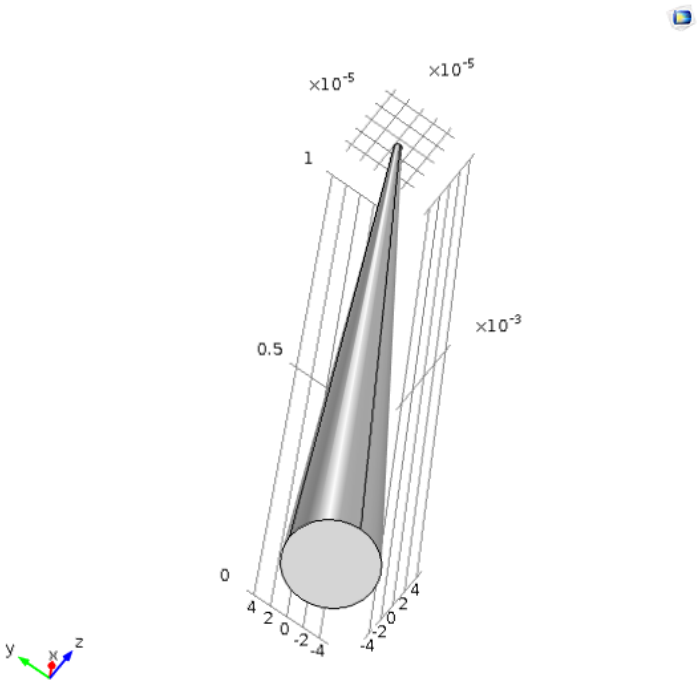

Figure 1.14: Trunk cone-shaped pipe as pictured by COMSOL Multiphysics®.

Material definition. The most common materials are already listed in a database, together with their main physical properties: such is the case for water. When added as a material, its dynamic viscosity and its density are automatically included in the model.

Studied phenomenon and boundary conditions. Choosing the phenomenon we want to study (creeping flow in our example) corresponds to stating the equations describing the phenomenon. For these equations to be (computationally) solved, starting and/or boundary conditions are needed. In our case, the biggest base of the trunk cone is designed as "Inlet"; the smallest, as "Outlet". These entities require a boundary condition, in our case the pressure existing on these surfaces (Δp on the inlet and 0 on the outlet). Finally, a "Wall" condition is imposed on the side surface of the cone (this turns into a "no-slip" condition: the fluid velocity is 0 at the walls).

Meshing. A mesh is created to divide the studied geometry into finite elements. The mesh can be automatically built in a way that is suitable for the physics of the problem ("Physics-controlled mesh"), or it can be more finely controlled by the user. The automatic method applied to our example yields the mesh shown in Figure 1.15.

Study selection. The type, or types, of study performed can be chosen. All throughout this work, we will consider stationary solutions only.

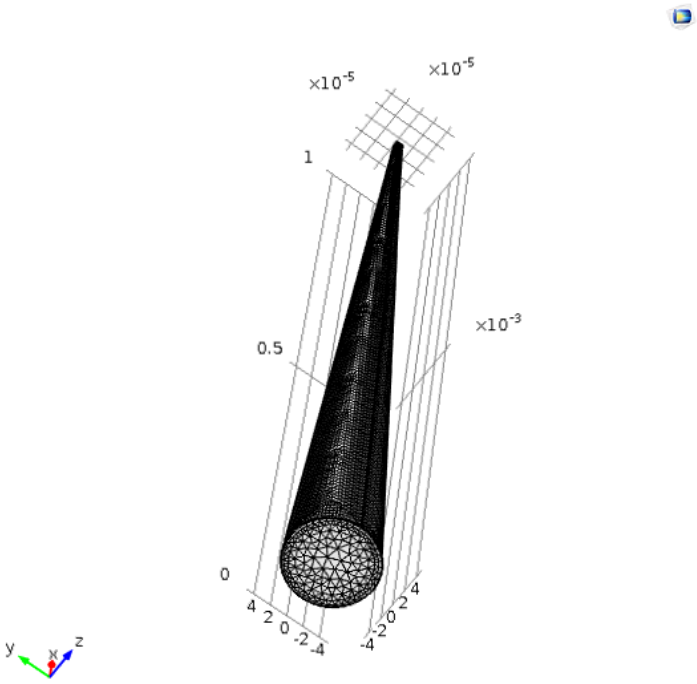

Figure 1.15: Physics-controlled mesh for the geometry presented in Figure 1.14.

After computing the solution for the model, various data sets are available, such as velocity magnitude maps on slices of the channel (Figure 1.16). For our purposes, we are here interested in the volume flow rate, that results constant all along the channel (as in Figure 1.17), consistently with Hagen-Poiseuille law. The values of Δp used as input and the correspondent flow rates Q obtained are listed in Table 1.1.

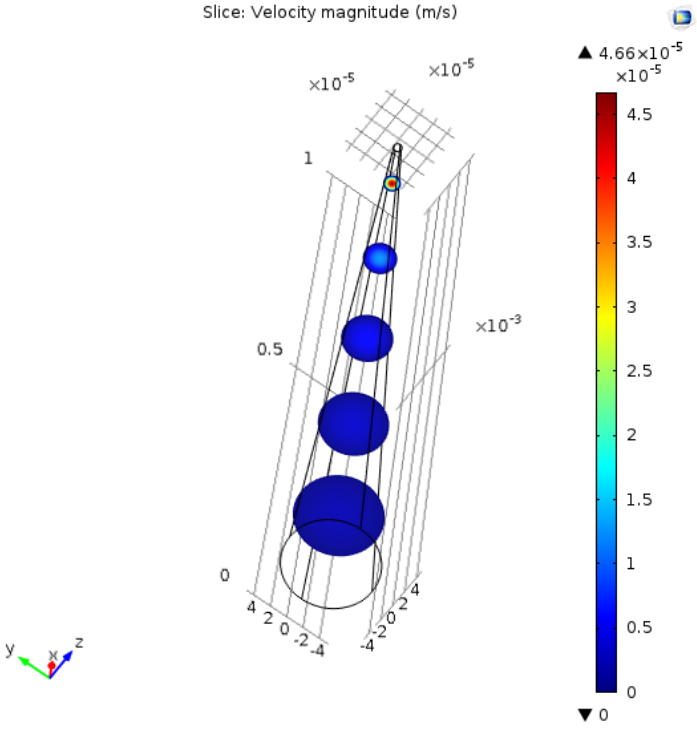

Figure 1.16: Velocity magnitude map on slices of the channel for $\Delta p = 1\,\mathrm{Pa}$.

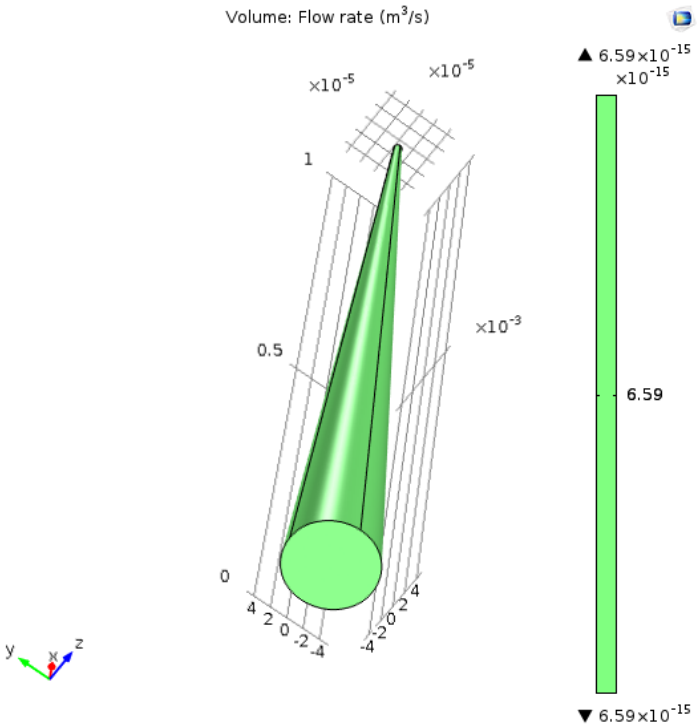

Figure 1.17: Volume flow rate map for $\Delta p = 1\,\mathrm{Pa}$.

Δp [Pa]	Q [^{3}m/s]
1	$6.59 \cdot 10^{-15}$
10	$6.59 \cdot 10^{-14}$
100	$6.59 \cdot 10^{-13}$
10^3	$6.59 \cdot 10^{-12}$
10^4	$6.59 \cdot 10^{-11}$
10^5	$6.59 \cdot 10^{-10}$
10^6	$6.58 \cdot 10^{-9}$

Table 1.1: Simulations results.

Chapter 2

Design of the microfluidic device

Once established the advantages of combining FCS detection with a flowing sample, and having examined the existing possibilities for the construction of a flow focusing microfluidic device, we can design our own device in detail. Our design shall meet the requirements dictated by the characteristics of the detection system, by the nature of the sample and by practical considerations. A preliminary way to test the effectiveness of the chosen focusing geometry is running a computer simulation of it; simulations can also help tuning the parameters of the fluid motion (such as volume flow rates) in order to optimize the system.

The design of our microfluidic device is described in Section 2.1. An explanation of how a flow was simulated in the chosen geometry can be found in Section 2.2, together with the results of such a simulation.

2.1 Chosen geometry and materials

The geometry for our device was chosen taking into account benefits and downsides of each of the options examined in Section 1.2.1. Additional factors that influenced our decision were the characteristics of the fabrication methods: they had to be feasible using the available instrumentation and machinery, and the resulting devices had to be reproducible. Moreover, the materials we would be using had to be compatible both with the sample and with the microscopy technique employed. Compatibility with the sample is particularly relevant when biological substances are studied, while the light emitted by the sample should obviously be altered as little as possible (ideally, not at all) before reaching the microscope: the device should have suitable optical properties.

A material that matches our requirements is poly(dimethylsiloxane) (PDMS), a biocompatible [16] elastomer. PDMS is transparent to visible and near-UV light [21]; moreover, its refraction index is $n = 1.430$, a (relatively) low value that reduces the amount of reflected excitation light in optical detection schemes [5]. This polymer can be used to build microfluidic devices employing affordable techniques that ensure replicability, namely soft lithography (see Section 3.1). This kind of fabrication is optimized to yield "two-dimensional" structures, that is, all the channels in a single PDMS slab have the same height. Multi-level soft lithography is possible as well, but it requires multiple alignments and exposures during mold fabrication [14], so that the complexity of the procedure grows with the number of different heights needed. In order to avoid multi-level soft lithography while keeping the structure of the device simple, we decided to make use of the coaxial capillaries geometry (that of method 1 presented in the previous section), embedding a thin glass capillary into a PDMS channel.

Glass is not as easy to manipulate as PDMS, but it features good optical properties and biocompatibility, too; moreover, it is possible to obtain glass capillaries with extremely thin diameters. In this, we benefited from the suggestions and expertise of prof. Erwin Neher (Max

Planck Institute for Biophysical Chemistry, Göttingen), who explained us that a pipette puller allows to get capillaries narrowing down from 100 µm diameter to 10 µm diameter. This helped us estabilishing our goal: a square cross-sectioned channel having two lateral inlets provided by an additional orthogonal channel and a central inlet made of a pulled capillary inserted into the central channel. To have the capillary coaxial to the central channel, the outer diameter of the former should match the side of the cross-section of the latter in dimension, at least in the position where the capillary enters the channel. For this reason, we aimed at a 100 µm × 100 µm cross-section for the PDMS channel, as illustrated in Figure 2.1. A sketch of the entire device structure can be find in Figure 2.2.

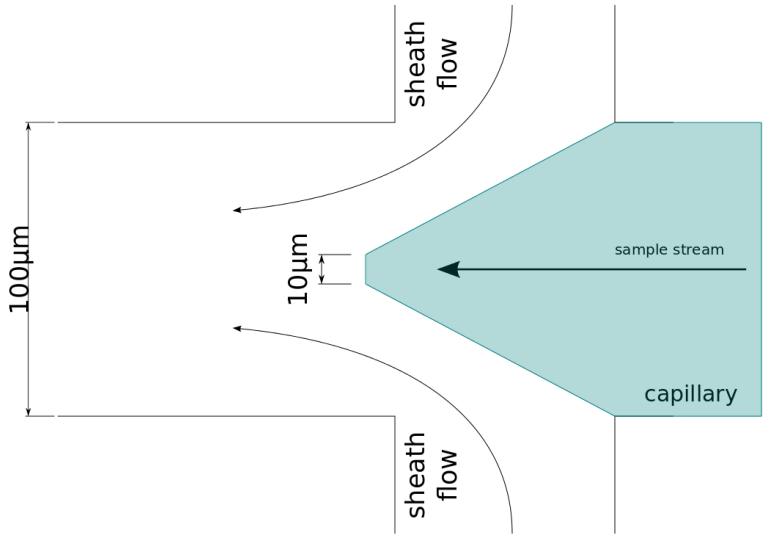

Figure 2.1: Top view of the chosen design, highlighting the most important dimensions (not to scale).

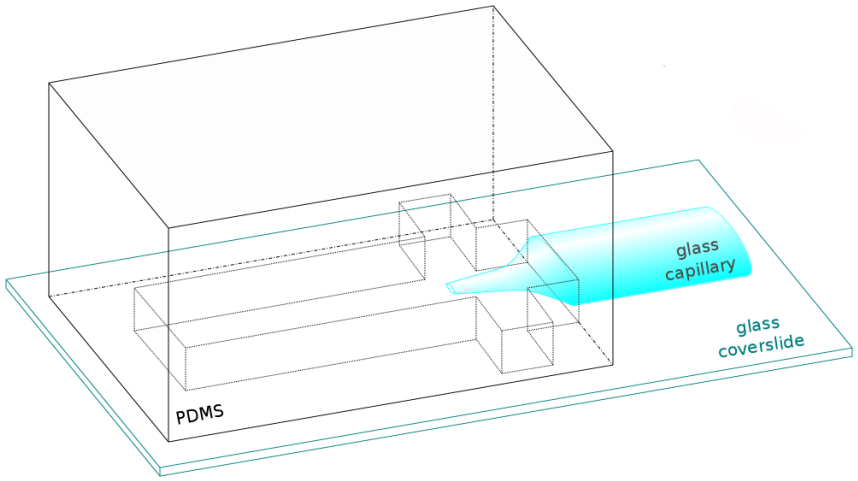

Figure 2.2: 3D view of the chosen geometry and materials (not to scale).

2.2 Simulations of the coaxial channels geometry

We can now have a first look at the validity of the geometry we chose with a FEM simulation. This will help us understand the flow focusing mechanism, determining which dynamic parameters one should choose, for the liquids entering the device, to obtain some target dimensions for the sample stream.

In order to reduce the computational time, the simulated geometry should be simplified as much as possible. First of all, since we are basically interested in what happens to the sample flow when it enters the main channel and gets sheathed by the focusing flow, we can limit our study to the stretch of the main channel beginning where the capillary ends, namely the region inside the green box in Figure 2.3. The tip of the capillary will be included just as a planar, circular inlet for the sample.

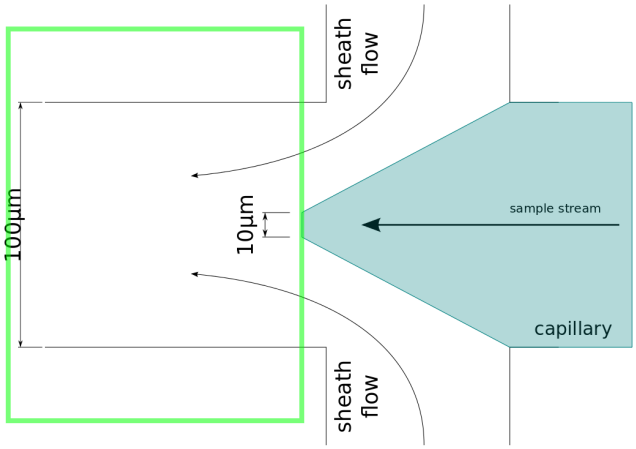

Figure 2.3: Top view of the chosen design. The green box highlights the portion of the channel to be simulated.

A further simplification is possible noticing the symmetry of the system: it is actually sufficient to simulate a quarter of the channel, as shown in Figure 2.4, to characterize all the flow properties.

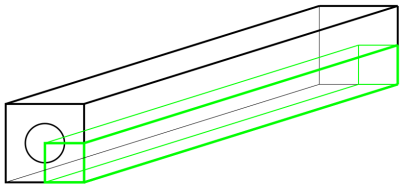

Figure 2.4: Stretch of the channel after the capillary end. The quarter to be simulated is highlighted in green.

The simulated geometry is therefore a rectangular cuboid, with a squared cross section of 50 µm side, 800 µm long, having the quarter of a 5 µm radius circle on one of its bases. The centre of the circle coincides with one of the corners of the base. The faces of the parallelepiped adjacent to the sides of this corner are those on which "symmetric" boundary conditions shall be imposed.

As model solutions, we used a 4 µM aqueous vimentin solution (diffusion coefficient $D_{\text{vim}} = 24 \cdot 10^{-12}\,\text{m}^2/\text{s}$) as the sample flow and a 100 mM aqueous KCl solution (diffusion coefficient $D_{\text{KCl}} = 1.6 \cdot 10^{-9}\,\text{m}^2/\text{s}$) as the sheath flow, but any other kind of solution could replace them, as long as the diffusion coefficients of the species considered are provided: in this way, the changes in concentration due to both diffusion and creeping flow motion can be computed (when using COMSOL, diffusion coefficients and initial concentrations are manageable using the "Transport of diluted species" menu).

We expect the characteristics of the flow to be regulated by the ratio r_{vel} of the linear velocities of the sheath and sample flows (v_{sheath} and v_{sample}, respectively):

$$r_{\text{vel}} = \frac{v_{\text{sheath}}}{v_{\text{sample}}}. \tag{2.1}$$

In order to verify this, ratios ranging from 0.05 to 8 are simulated. However, instead of linear velocities, we use the initial flow rates as boundary conditions at the inlet, since those are the parameters we can control in the experiments (see Section 3.1.4). Sheath flow rates range from $Q_{\text{sheath}} = 200\,\mu\text{L/h}$ (a common value in the applications) to $Q_{\text{sheath}} = 3600\,\mu\text{L/h}$ (quite a high value); sample flow rates are chosen accordingly, so that the velocity ratio is the desired one. This can be done assuming a constant linear velocity for each inlet, so that the volume flow rate Q in a channel of cross section S can be related to the velocity v of the same flow as $Q = v \cdot S$. The complete list of inputs can be found in Table A.1 (in Appendix A), together with the corresponding velocities and velocity ratios. It is important to recall that the real velocity profile is parabolic: another interesting possibility offered by simulations is that of comparing the velocities computed as described with the more realistic values yielded by the numerical solution of the hydrodynamic equations.

Three dimensional plots of the simulation results help making some first, qualitative considerations. The velocity magnitude and field (Figure 2.5) resemble that of a Poiseuille flow in a squared channel (the parabolic profile, typical of cylindrical channels, is modified near the walls of the squared channel), after a not so long initial stretch of channel near the inlets, where the influence of the velocity difference between sample and sheath flow is stronger.

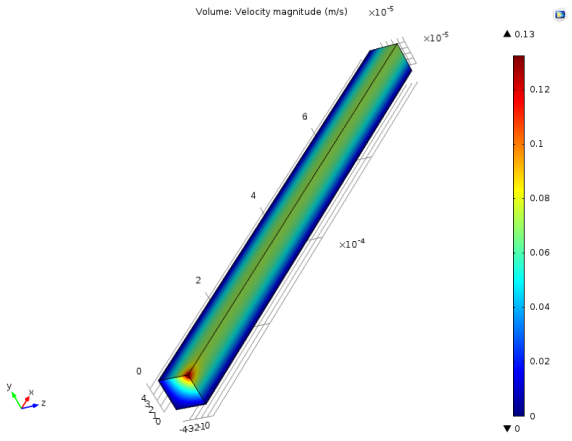

(a) *Sample flow rate:* 7.92 µL/h *(corresponding to* 31.7 µL/h *in the complete channel). Sheath flow rate:* 300 µL/h *(corresponding to* 1200 µL/h *in the complete channel).*

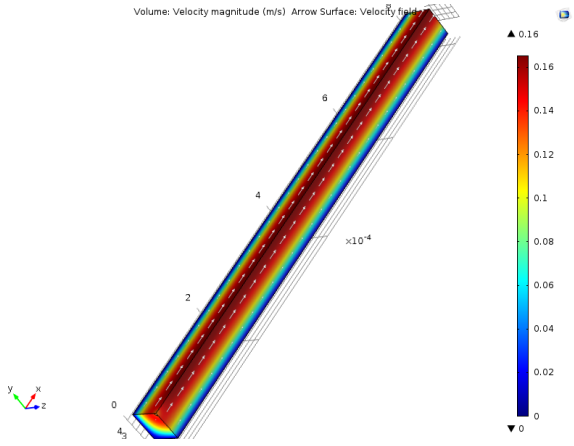

(b) *Sample flow rate:* 7.92 µL/h *(corresponding to* 31.7 µL/h *in the complete channel). Sheath flow rate:* 700 µL/h *(corresponding to* 2800 µL/h *in the complete channel).*

Figure 2.5: Velocity magnitude plots in the simulated volume.

The concentration of the sample (vimentin) flow shows that a constriction for it is indeed achieved (Figure 2.6). When raising the value of the sheath flow rate, it becomes more and more difficult to visualize the shape of the sample flow in this kind of plot, because the concentration becomes very low.

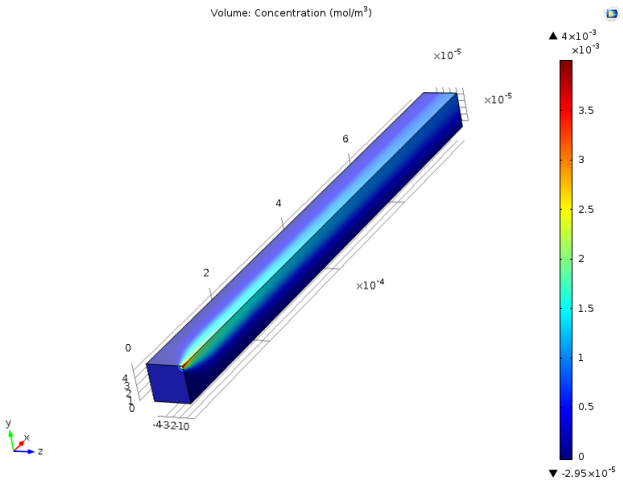

Figure 2.6: Sample concentration in the simulated volume, for a 7.92 µL/h sample flow rate (31.7 µL/h in the complete channel) and a 50 µL/h sheath flow rate (200 µL/h in the complete channel).

More quantitative conclusions can be drown from unidimensional plots. Let us first have a look to the velocity magnitude in the middle axis of the (complete) channel, along the axis itself (Figure 2.7). In this plot, we can clearly see how the velocity reaches a constant value in less than 100 µm, thus confirming our observations on the three dimensional velocity distribution. The velocity has to reach its constant value either decreasing (Figure 2.7a), for the simulations corresponding to an expected velocity ratio $0.05 \leq r_{\text{vel}} \leq 0.5$, or increasing (Figure 2.7b), for the simulations corresponding to an expected velocity ratio $0.6 \leq r_{\text{vel}} \leq 8$.

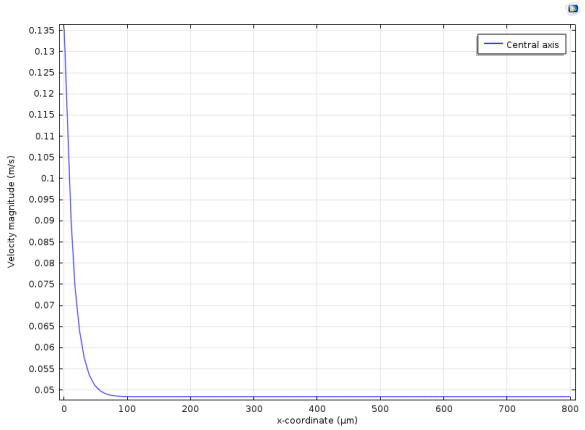

(a) *Sample flow rate:* 7.92 µL/h *(corresponding to* 31.7 µL/h *in the complete channel). Sheath flow rate:* 200 µL/h *(corresponding to* 800 µL/h *in the complete channel).* $r_{vel} = 0.2$.

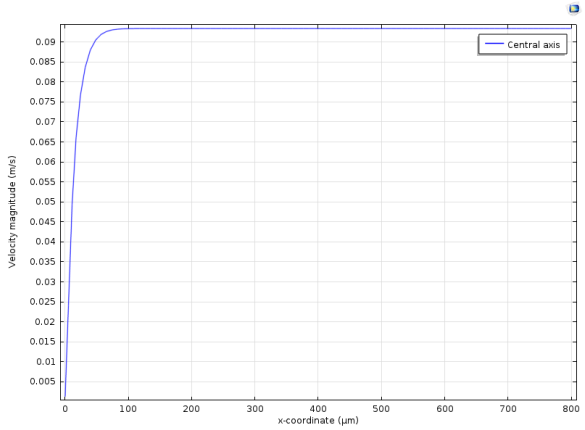

(b) *Sample flow rate:* 0.79 µL/h *(corresponding to* 3.17 µL/h *in the complete channel). Sheath flow rate:* 400 µL/h *(corresponding to* 1600 µL/h *in the complete channel).* $r_{vel} = 1$.

Figure 2.7: Middle velocity profile along the x-axis.

A relation can be searched between the input parameters and the constant velocity displayed in this kind of plots. A way to consider both the sample and the sheath flow rates used as

inputs is that of summing them and then estimating a mean velocity v_{ch} for the whole channel as the ratio of this total flow rate and the cross sectional area S_{ch} of the channel:

$$v_{\text{ch}} = \frac{Q_{\text{sample}} + Q_{\text{sheath}}}{S_{\text{ch}}}. \tag{2.2}$$

We expect this mean velocity to be smaller than the constant velocity v_{const} resulting from the simulations, since the latter is the maximum velocity rather than a mean velocity. When plotting the percent difference between these two velocities, $(v_{\text{const}} - v_{\text{ch}})/v_{\text{const}} \cdot 100$, against the expected velocity ratio r_{vel}, that is revealed to be chiefly constant, as Figure 2.8 shows. We can then assume a mean difference of $(52 \pm 2)\%$ and use it to predict the maximum velocity v_{const}, given v_{ch}.

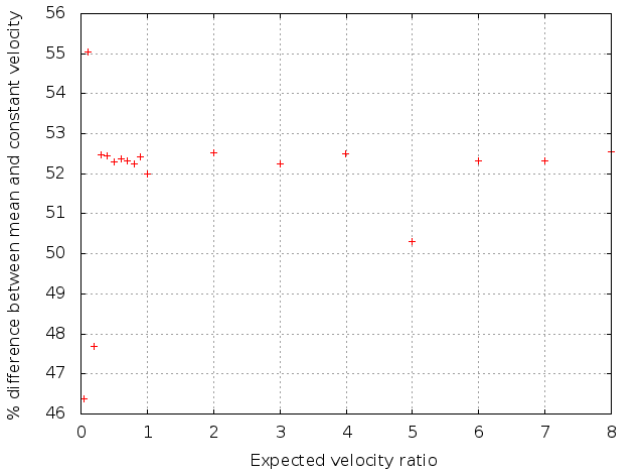

Figure 2.8: Percent difference between v_{const} and v_{ch} *versus* r_{vel}.

A further confirmation of the establishment of a Poiseuille velocity profile in the channel is given by the velocity magnitude radial distribution (Figure 2.9): different cross sections of the channel are individuated by their x coordinate, and for each of these planes the evolution of the velocity magnitude along the diagonal of the cross section is considered (each cross section is a square; the diagonal used as the abscissas axis is the one starting in the middle of the complete channel and reaching the corner formed by the external walls). While the velocity magnitude depends not only on the radial coordinate, but also on the x coordinate (Figures 2.9a and 2.9b), the dependence on x disappears for $x \gtrsim 100\,\mu\text{m}$ (Figure 2.9c).

Vimentin concentration in the middle of the complete channel decreases along the x-axis, while its concentration at the walls slightly increases, due to its diffusion, mostly happening in the radial direction (Figure 2.10). The radial distribution of the concentration (Figure 2.11) gives us a better idea of the sample stream dimensions.

The high steepness of the curves shown in Figure 2.11 mean that the sample stream is well focused. Taking a constant concentration value as a reference, it is possible to measure the corresponding radius on different x = constant planes, thus visualizing how the focusing varies along the x-axis. This is shown in Figure 2.12, for a concentration value equal to 5% of the initial value when $Q_{\text{sample}} = 7.92\,\mu\text{L/h}$ (Figure 2.12a), to 0.5% of the initial value when $Q_{\text{sample}} = 0.792\,\mu\text{L/h}$ (Figure 2.12b). These reference values of the concentrations were chosen only to make the radii measurements easy and have no particular physical meaning. The shape of the sample stream is nonetheless clear: our geometry produces a constriction that tends to be less pronounced for higher x values, because the focusing is contrasted by molecular diffusion. For high sheath flow rates (here corresponding to velocity ratios 0.2, 0.3, 3, 4, 5 and 6), the sample stream radius initially increases, but then decreases again along the x-axis, because the

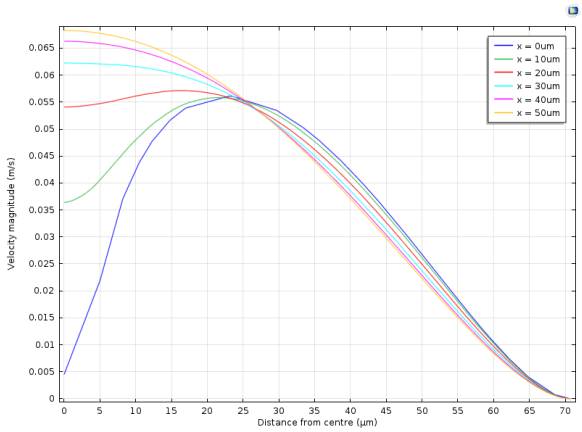

(a) *Radial velocity,*
$0\,\mu\text{m} \leq x \leq 50\,\mu\text{m}$.

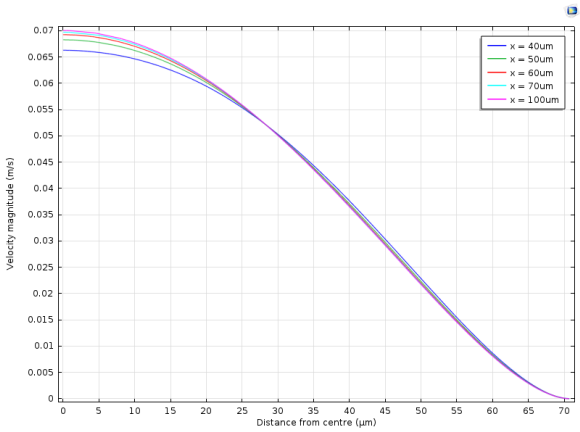

(b) *Radial velocity,*
$40\,\mu\text{m} \leq x \leq 100\,\mu\text{m}$.

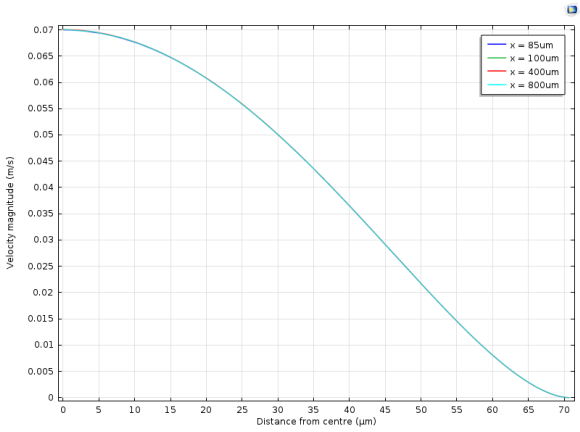

(c) *Radial velocity,*
$85\,\mu\text{m} \leq x \leq 800\,\mu\text{m}$.

Figure 2.9: Radial distribution of the velocity magnitude for a 0.79 µL/h sample flow rate (corresponding to 3.17 µL/h in the complete channel) and a 300 µL/h sheath flow rate (1200 µL/h in the complete channel).

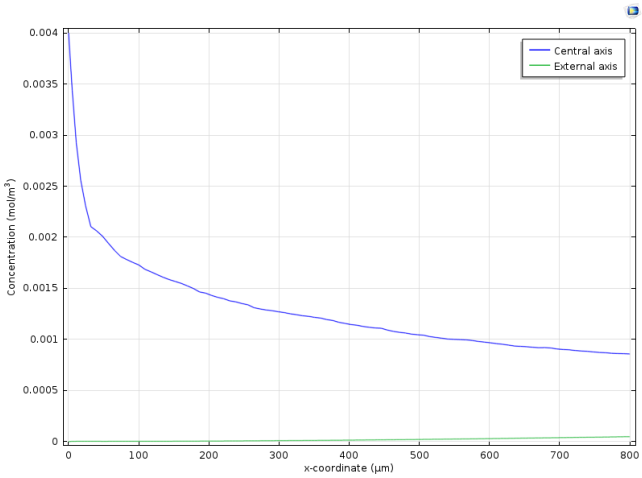

Figure 2.10: Sample concentration along the x-axis, in the middle and at the walls of the channel. Sample flow rate: 7.92 µL/h (31.7 µL/h in the complete channel). Sheath flow rate: 50 µL/h (200 µL/h in the complete channel).

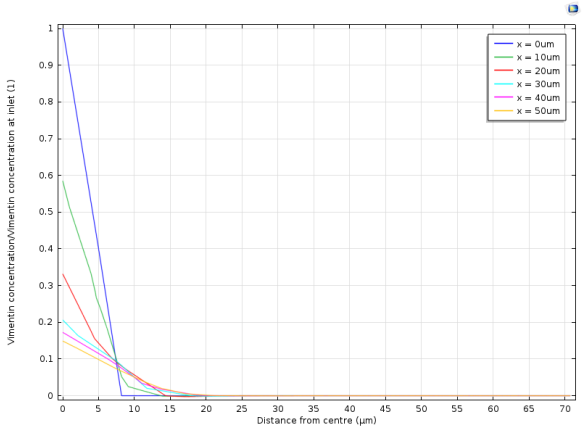

(a) *Radial concentration,* $0\,\mu\text{m} \leq x \leq 50\,\mu\text{m}$.

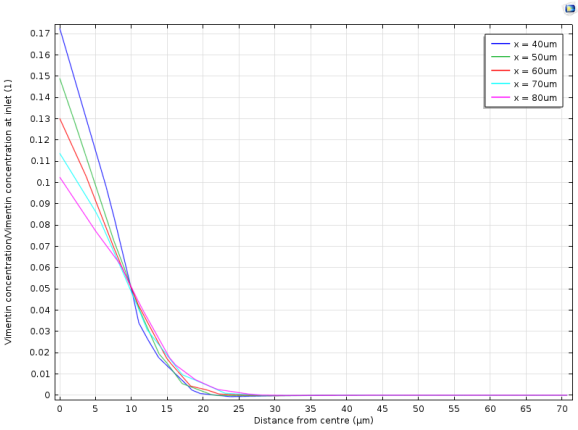

(b) *Radial concentration,* $40\,\mu\text{m} \leq x \leq 800\,\mu\text{m}$.

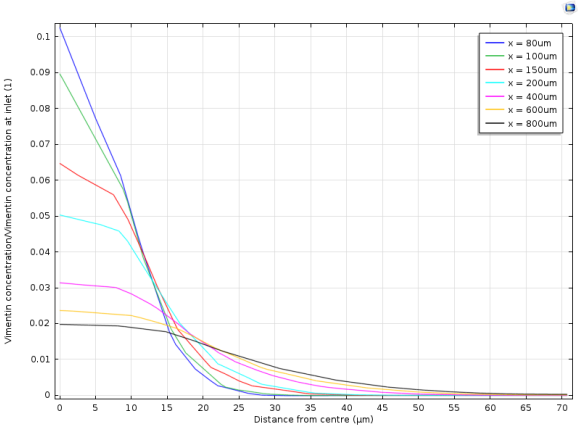

(c) *Radial concentration,* $80\,\mu\text{m} \leq x \leq 800\,\mu\text{m}$.

Figure 2.11: Radial distribution of the sample concentration. Concentration values are given as a fraction of the concentration at the inlet (4 µM), to better see the focusing capabilities, regardless of the initial conditions. Sample flow rate: 7.92 µL/h (31.7 µL/h in the complete channel). Sheath flow rate: 800 µL/h (3200 µL/h in the complete channel).

higher sheath solution volume present in the system strongly dilutes the sample, so that the sample concentration dramatically decreases in the radial direction.

We finally mention that the use of different solutes for the sample (vimentin) and the sheath (KCl) flows enable to study the mixing capabilities of the device: because of radial diffusion, the sample concentration in the middle of the channel decreases, while that of the sheath solution increases, along the x-axis (Figure 2.13). Once more, concentrations are given as fraction of their respective values at the inlets, otherwise they would not be clearly visible on the same plot, because the absolute value of the sample solution concentration is extremely lower than that of the sheath solution. The point where the two curves meet depends on the flow rates: mixing is faster for higher flow rates.

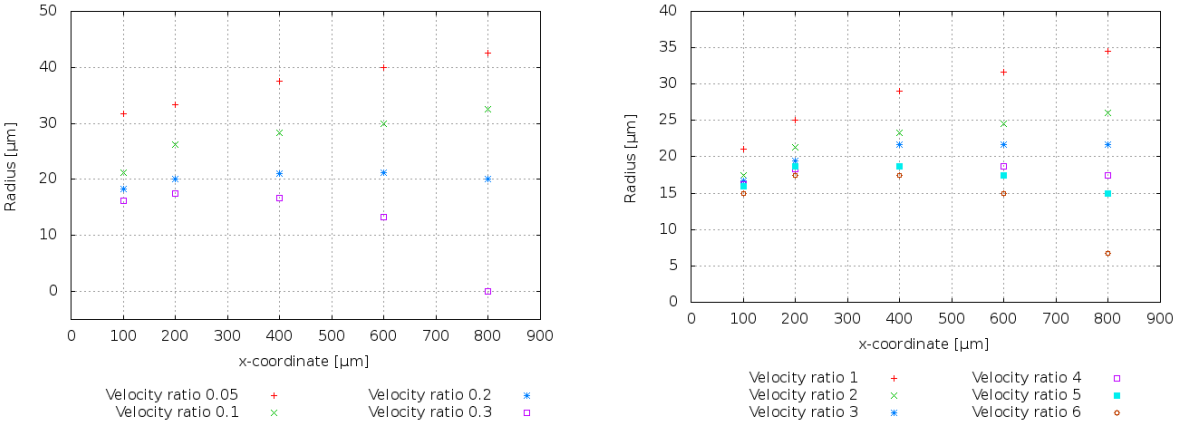

(a) *Sample flow rate:* 7.92 µL/h. (b) *Sample flow rate:* 0.79 µL/h.

Figure 2.12: Sample stream radius dependence on the x coordinate for different expected velocity ratios r_{vel}.

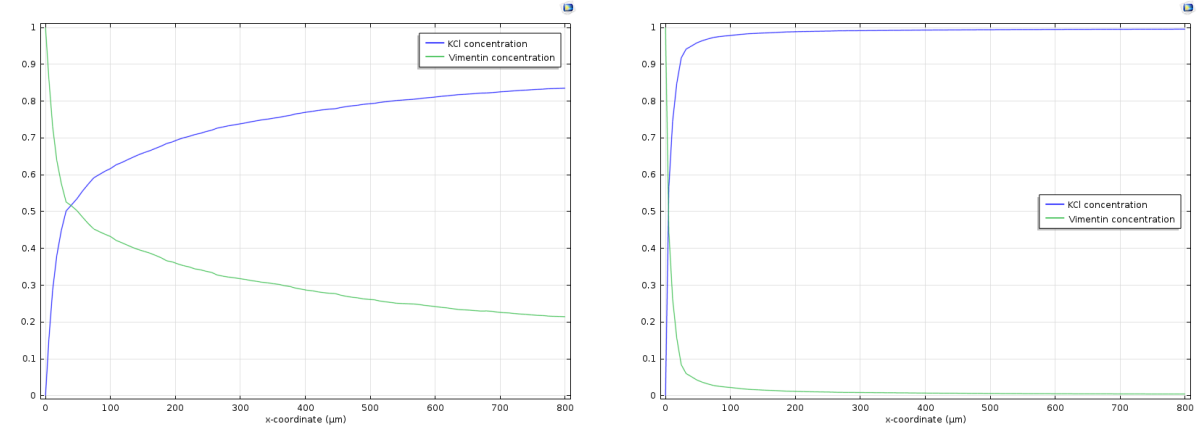

(a) *Sample flow rate:* 7.92 µL/h*; sheath flow rate:* 50 µL/h. (b) *Sample flow rate:* 0.792 µL/h*; sheath flow rate:* 800 µL/h.

Figure 2.13: Evolution of the concentration of the two solutes considered, in the middle of the channel, along the x-axis.

Chapter 3

Experimental approach

Once established the characteristics that the microfluidic device should have, it is possible to actually build it. All components have to be crafted and put together, then the effectiveness of the device can be tested. Instead of directly making a device with the dimensions examined in Section 2.1, we proceeded gradually, first building devices with bigger channels, then testing them, and subsequently making the next device smaller. In order to appreciate the focusing capability of a device, the width of the sample streams shall be measured. Moreover, to validate their use in the development of the device, simulations such as those described in Section 2.2 have to be compared with the experimental results.

The materials and methods employed both in the construction and in the experimental examination of the devices are described in Section 3.1, while an account of the experimental examination itself can be found in Section 3.2. A comparison between experimental data and simulation results is the subject of section 3.3.

3.1 Materials and methods

3.1.1 Soft lithography

The channels needed for the microfluidic devices are made out of PDMS, which forms three out of four walls (the fourth wall is obtained by sealing the channels with a glass cover slide), using *soft lithography*.

The PDMS is cast against a master fabricated *via* photolithography, which carries the channels features in high relief. Specifically, a photoresist is spincoated on a silicon wafer, obtaining a uniform layer, as thick as the desired channel height. The shape of the channel network is designed using a CAD program and printed on a trasparency: this yields a mask that is superimposed on the photoresist. When illuminating by UV light, the illuminated areas are crosslinked, while the rest of the photoresist, covered by the mask, is not, and can be removed with a solvent. The procedure described so far is carried out in a clean room, while all the following operations do not have this requirement. The resulting mold is put in a desiccator with Heptafluoro-propyl-trimethylsilane, so that the PDMS can be easily peeled away; the master can be reused many times (ideally, indefinitely). These preliminary steps, necessary to obtain the silicon molds and requiring $2 \div 3$ hours for each wafer, have not been performed by the writer. A scheme of the procedure can be seen in Figure 3.1.

Once the mold is ready, a mixture of $10 : 1$ (in weight) PDMS prepolymer and crosslinker (Sylgard® 184 Silicone Elastomer, Dow Corning GmbH, Wiesbaden, Germany) can be poured into it. The PDMS is then degassed in a desiccator; when no more bubbles are visible, it is cured in an oven at 65 °C for at least 3 hours. After that, the PDMS slab, now carrying the channels design in low relief, can be cut with a scalpel and peeled away from the silicon wafer.

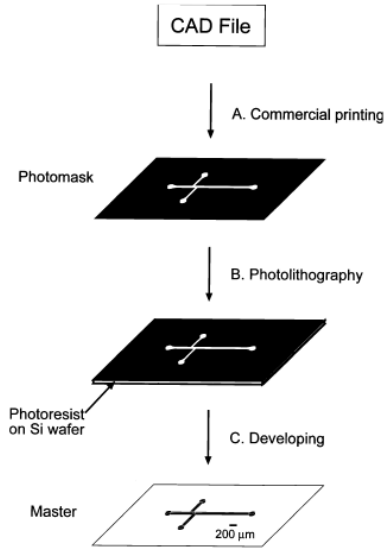

Figure 3.1: Soft lithography scheme from McDonald et al.'s article on PDMS microfluidic devices [16]. (a) A design for channels is created in a CAD program. (b) This file is printed on a high-resolution transparency. (c) The transparency then serves as the photomask in contact photolithography. (d) Dissolving away the unpolymerized photoresist leaves a positive relief that serves as a master.

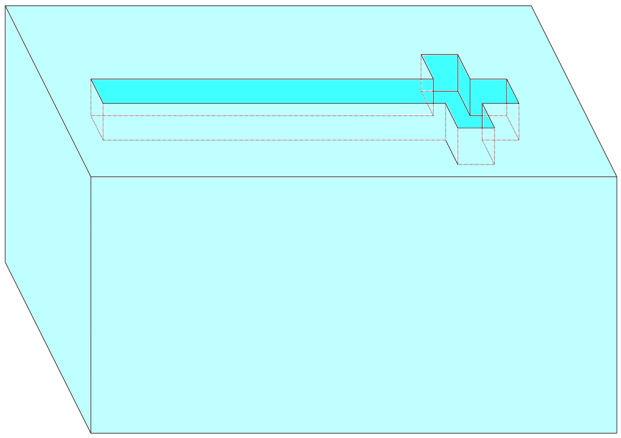

Figure 3.2: Example of channels in PDMS bulk obtained by soft lithography.

The featured PDMS slab thus obtained can be used either as a component for the device we intend to create, or as a mold for the construction of a new master: for the second purpose, the PDMS slab (cleaned with isopropanol and blown dry with nitrogen) is placed into a Petri dish and put into a plasma cleaner (PDC-32G, Harrick Plasma, Ithaca, USA); the channels are exposed to an air plasma for 30 s. After that, it is transferred to a desiccator, together with 40 µL of HMDS (hexamethyldisilazane). The desiccator is evacuated for 20 s, then disconnected from the pump and left closed for at least 10 min, so that the HMDS coats the slab. Now, pre-degassed PDMS can be poured into the Petri dish; then, it is degassed again and finally baked at 65 °C for just an hour, so that the new PDMS slab is easier to peel out. This new slab has the channels in high relief, just like the original silicon master, and can be used as a mold following the PDMS-PDMS copy procedure just described. Such a procedure is a bit more time consuming than using the silicon wafer, because of the HMDS coating, and PDMS surfaces are more difficult to clean than silicon ones; on the other hand, PDMS molds are less fragile than silicon wafers, and the photoresist tends to release from the wafer itself after several uses. PDMS masters are therefore useful when access to new silicon molds is limited.

3.1.2 Capillary pulling

A horizontal pipette puller (H. Saur Laborbedarf, Reutlingen, Germany) is used to reduce the diameter of a glass capillary. The two ends of the capillary are fixed and its middle is heated by a ring-shaped electrical resistance, experiencing Joule effect, that surrounds it. During the heating, one of the two ends of the capillary is pulled away from the other, so that the capillary lengthens and thins down (Figure 3.3).

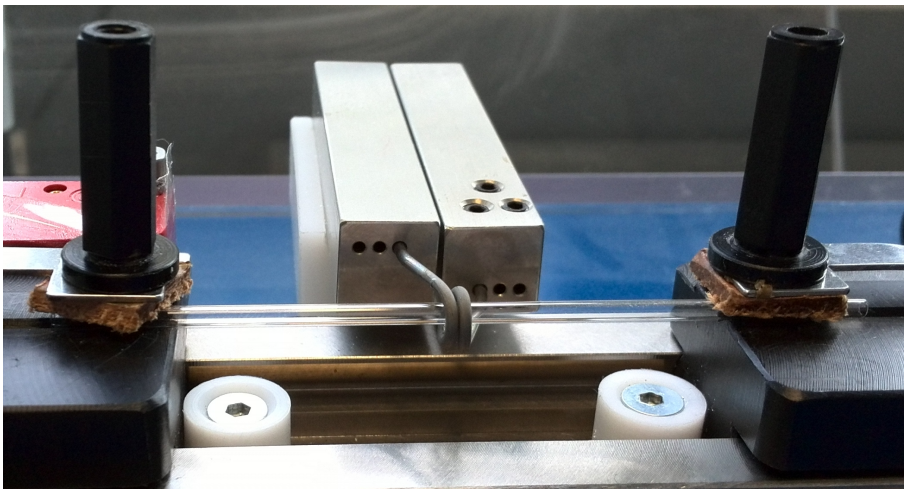

(a) 2 mm *diameter capillary ready to be pulled.*

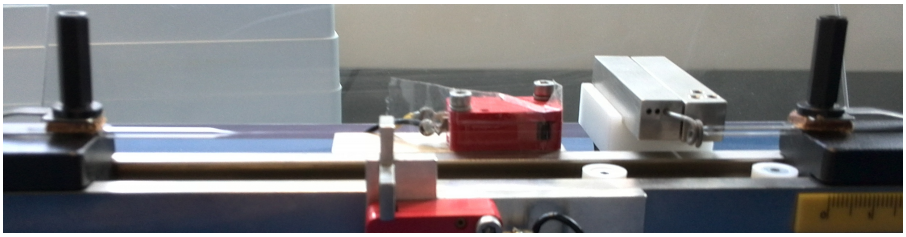

(b) 2 mm *diameter capillary right after pulling.*

Figure 3.3: 2 mm diameter capillary set in the pipette puller.

Though the pipette puller is designed to pull glass pipettes having a 2 mm initial outer diameter, it can also be used for much thinner capillaries (80 mm long; 0.10 mm outer diameter; 0.01 mm wall thickness – Mark-tubes made of soda lime glass, Hilgenberg GmbH, Malsfeld, Germany), provided that the sites for the capillary ends are adjusted to host a 100 µm diameter capillary (we simply add some folded paper to fill said sites): the slightly different set-ups of the machine can be seen comparing Figures 3.3 and 3.4. Since the thinner capillaries were the only ones available at the beginning, the majority of the devices was made with them.

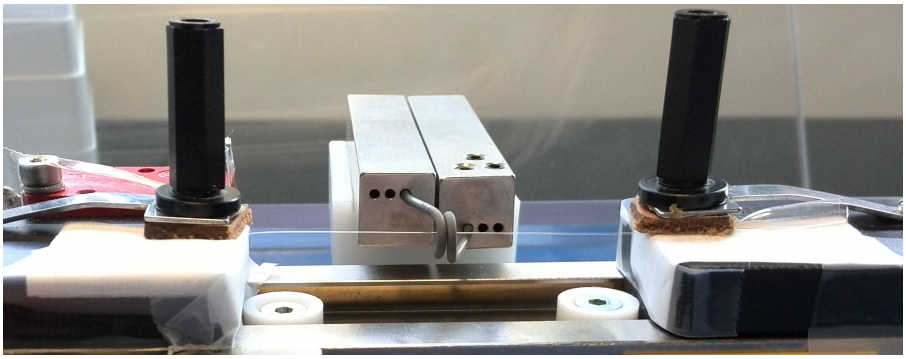

Figure 3.4: 100 µm diameter capillary set in the pipette puller.

The final dimensions of the capillary can not be precisely selected: tip diameters range from about 50 µm to about 10 µm, and longer capillaries usually – but not always – have thinner tips. The desired diameter can be picked by measuring the capillary diameter at different positions using a stereomicroscope (Olympus SZ61), locating the point where the wanted size is assumed and cutting the capillary there. The cut is made using a pair of thin tweezers and bending the capillary until the unwanted tip is torn apart, so the result is a rough cut.

3.1.3 Assemblage of the device

A punch (Biopsy Punch, World Precision Instruments Ltd., Hitchin, UK) is used to form holes in the PDMS slab obtained from soft lithography: the holes are positioned at the ends of the lateral inlets and at the outlet of the channel network; they will provide the sites for the tubing used to deliver fluids into the device and to bring waste away. The diameter of the holes is 0.75 mm, smaller than the 1.09 mm outer diameter of the tubing: this ensures a tight, leakage-free connection.

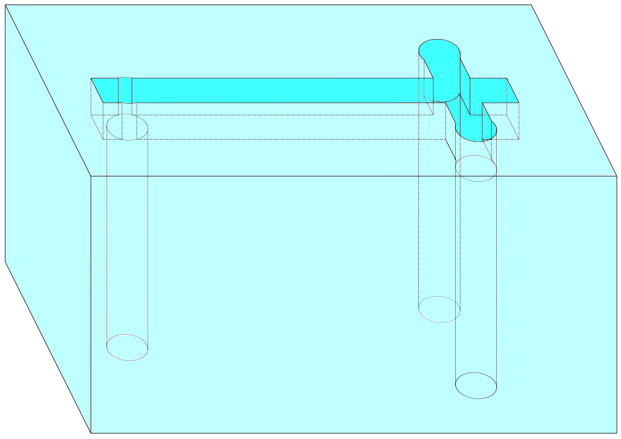

Figure 3.5: Scheme of the PDMS slab with inlet and outlet holes.

After that, a cut orthogonal to the central channel is made, so that only a stretch of central channel shorter than 1 mm is left before the junction with the lateral inlets. When needed, the slab is cut further on its other sides, so that it fits on a glass coverslide (24 mm × 60 mm). In order to make straight, sharp cuts, a straight piece of cardboard is used as a ruler to guide the scalpel blade.

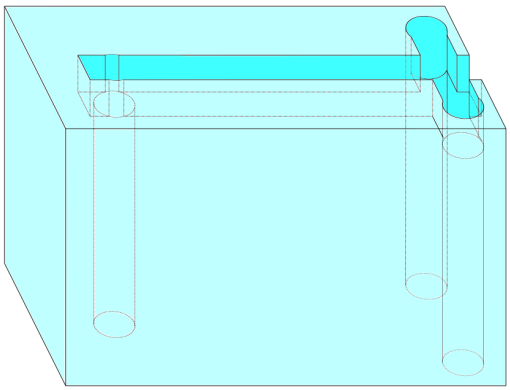

Figure 3.6: Scheme of the PDMS slab after cutting it out.

The PDMS slab and a glass coverslide are then rinsed with isopropanol, blown dry with nitrogen and placed on the hot plate at 95 °C for a few minutes, to let any residual isopropanol evaporate. Both items are put in the plasma cleaner for 10 s, making sure to expose the channels (and not the opposite side of the slab). The coverslide is then placed on the hot plate again, and the PDMS is pressed against it for approximately one minute, so that the sides exposed to the plasma bond. This kind of bond is permanent, and it makes the walls of the channels hydrophilic [16].

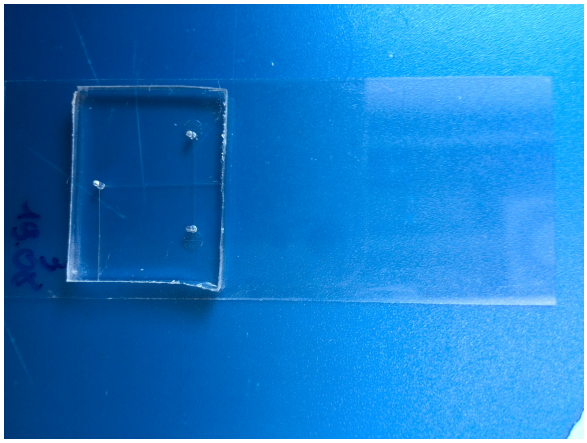

(a) *Picture of a device sealed with a coverslide.*

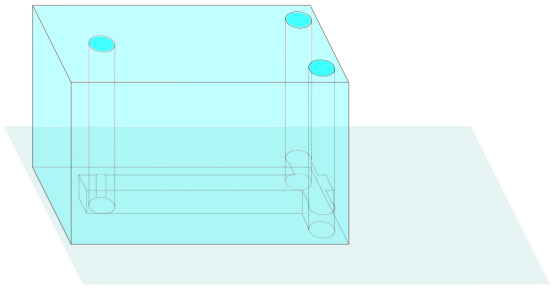

(b) *Scheme of a device sealed with a coverslide.*

Figure 3.7: Example of a glass-sealed device.

The next step is the insertion of a (pulled) glass capillary inside the central channel. This is accomplished under a stereomicroscope (Olympus SZ61), making the capillary slide through the channel until its tip gets past the channel junction. When the desired position is reached, the capillary is fixed on the coverslide by putting a drop of two-component glue (UHU® Plus Sofortfest or UHU® Plus Schnell Fest, UHU GmbH & Co., Bühl, Germany) at the entrance of the main channel. The glue takes an hour to dry, at room temperature, after which the device is ready to use.

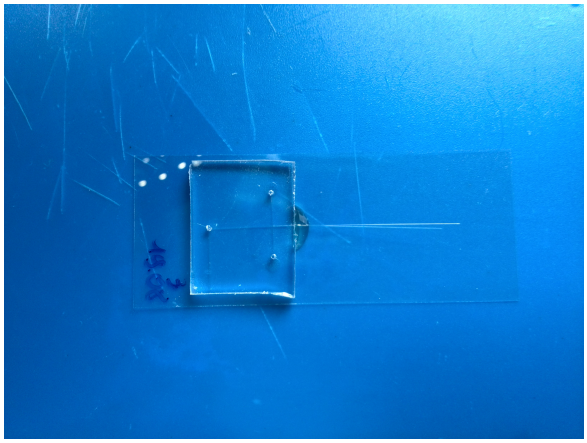

(a) *Picture of a completed device: the capillary forms the central inlet.*

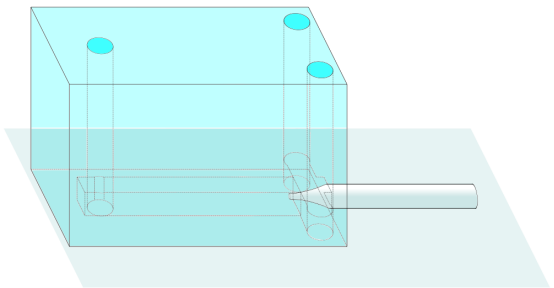

(b) *Scheme of a completed device.*

Figure 3.8: Example of completed device.

Leaving only a short stretch of main channel before the junction works very well for capillaries that narrow down from $\approx 100\,\mu m$ diameter to $\approx 10\,\mu m$ diameter in a short distance ($\lesssim 1\,mm$): such is the case for the devices kindly provided by prof. Neher's group. As can be seen in Figure 3.9, these capillaries are very well centered into the main channel.

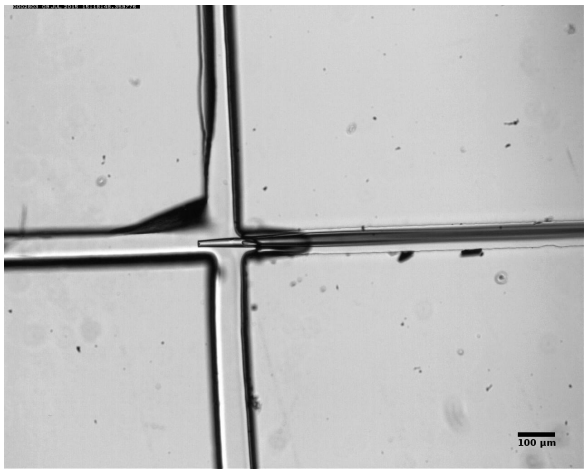

(a) *First device provided by prof. Neher's group.*

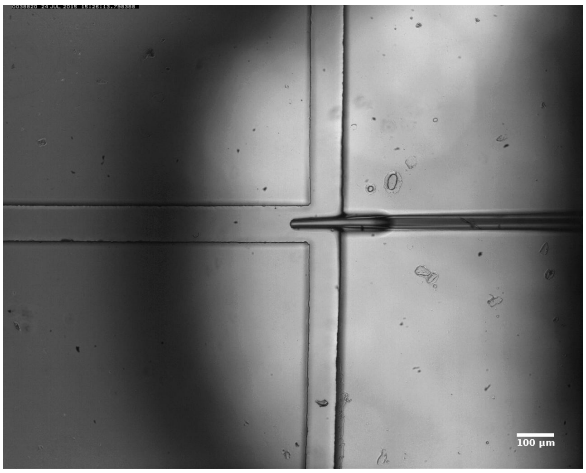

(b) *Second device provided by prof. Neher's group.*

Figure 3.9: Devices provided by prof. Neher's group: both glass-sealed devices were made by the writer; the capillaries were pulled and inserted into the device by prof. Neher's group.

Our capillaries, however, thin down along much longer distances, ranging from millimetres to few centimetres: this increases both the difficulties in centering the capillary and the risk that the glue enters the device and clogs it. In order to solve these issues, longer stretches of central channel have been left before the junction. First, each capillary is measured using the stereomicroscope, to know the length along which the diameter changes from 100 µm to 10 µm. These measurements are performed before cutting the PDMS slab: this allows us to leave, before the junction, a stretch of main channel approximately 1 mm shorter than the aforementioned measured length, so that the diameter of the capillary matches the channel size in the position where it enters the channel itself, which should result in a good centering and prevent the glue from reaching the channels junction. This expedient, however, does not entirely solve our problems: the long, thin tips of the capillaries are extremely flexible, and they tend to stick to the PDMS walls of the channel, so that making them slide through the channel becomes tricky. A drop of isopropanol, placed at the very entrance of the central channel, can help in this procedure: because of capillarity, the drop enters both the channel and the capillary, preventing the tip of the latter from getting stuck or bending. Afterwards, in order to make the isopropanol evaporate, the device has to be put on the hot plate (at 95 °C). Since such evaporation can cause a displacement of the capillary, this is glued onto the device *before* putting all on the hot plate. This sometimes prevents the glue from hardening properly. It is also worth mentioning that good centering is still not certain: whenever the capillary is not straight, either due to the pulling procedure (Figure 3.10a) or to bending inside the channel (Figure 3.10b), its tip ends up touching one of the walls (Figure 3.10c).

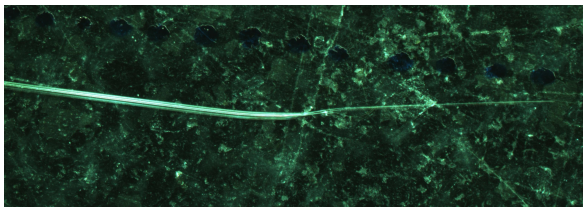

(a) *After pulling, the capillary is not straight anymore.*

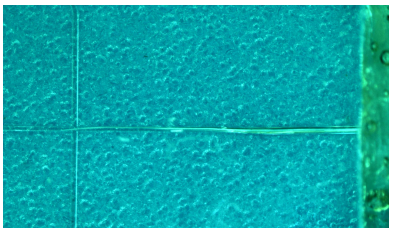

(b) *The capillary can also bend when inserted into the PDMS channel.*

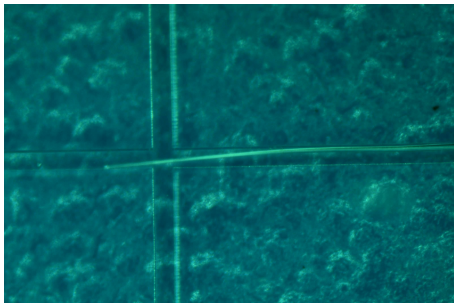

(c) *This capillary is not centered: its tip touches one of the walls.*

Figure 3.10: Issues in capillary centering.

3.1.4 Fluid delivery system

Syringe pumps (neMESYS Low Pressure Module, cetoni GmbH, Korbussen, Germany) deliver the outer flow into the device: the distilled water used as sheath flow is stored into two identical syringes (Hamilton Gastight #1001, 1 mL volume, 4.607 mm inner diameter, or #1005, 5 mL volume, 10.301 mm inner diameter – Hamilton Bonaduz AG, Bonaduz, Switzerland), one for each lateral inlet. Each syringe terminates with a 0.40 mm diameter needle, stuck into a piece of tubing (0.38 mm inner diameter, 1.09 mm outer diameter – Intramedic™ Clay Adams™ polyethylene tubing, Sparks, USA). The pumping system makes the piston of each syringe move at a constant speed: as a consequence, water is injected into the tubing at a constant volume rate. The free end of the tubing is pushed into a lateral inlet hole. Such a connection is tight enough to avoid leakages.

This constant-volume-rate-based method can also be used for the sample solution, as long as the diameter of the capillary is no less than $\approx 50\,\mu$m: in this case, the capillary end that is outside the PDMS channel is inserted into the tubing and the link is secured with a drop of the same two-components glue used to fix the capillary to the coverslide. When working with thinner diameters, such a system experiences leakages, or even the rupture of the capillary: it is then appropriate to drive the flow by applying a constant pressure. This can be actualised putting the sample solution into a reservoir (e.g. a beaker), placing it higher than the capillary, and connecting reservoir and capillary with a piece of tubing: calling h the height of the liquid column obtained (measured from the plane where the capillary lies to the level of the liquid-air interface into the beaker) and ρ the density of the liquid, the hydrostatic pressure at the base of the column equals

$$\Delta p = \rho g h \tag{3.1}$$

(g is the gravitational acceleration). In order to waste a lesser amount of sample, the beaker can be substituted by a syringe without piston, attached to a tap (one of those also used for chromatography columns) that has a syringe needle on its other end: the needle can be inserted into the tubing, and then glued to the capillary as usual. The tap allows to start or stop the

flow when needed (Figure 3.11).

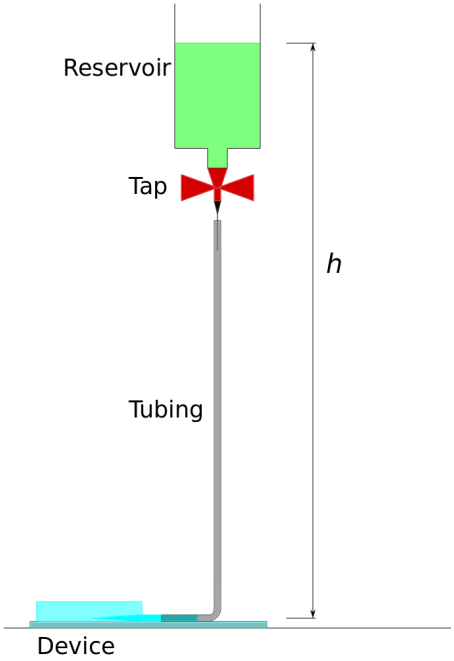

Figure 3.11: "High reservoir" fluid delivery system.

When capillaries with a 2 mm diameter are employed, only a bigger tubing (2 mm inner diameter, 2.8 mm outer diameter – Deutsch & Neumann GmbH, Berlin, Germany) can be attached to them. This big tubing is connected to standard 0.38 mm diameter tubing using an "adaptor" made of PDMS: the latter is merely a straight channel beginning with a 2.5 mm diameter hole (for the thick tubing; made using a Harris Uni-Core^{TM} Punch, Ted Pella Inc., Redding, CA, USA) and ending with a 0.75 mm diameter hole (for the thin tubing). The fourth wall of the channel is made of PDMS, too: the slab carrying the channels is sealed using the same procedure described in Section 3.1.3 for PDMS-glass bonding, only replacing the coverslide with a plain, non-featured slide of PDMS.

Filling the capillary up to its tip becomes critical when dealing with such small dimensions. Watery solutions can fill a horizontal capillary thanks to capillary pressure only, but not very fast; in addition, as soon as an air bubble is trapped in the liquid bulk, the process slows down so much as to prevent experiments. To reduce filling times, the piece of tubing and the capillary should be filled *before* being attached. This is easily done for the tubing using a syringe (or a pipette in the case of a thick tubing), while for capillaries it is more tricky and time consuming.

The strategy used for the thin capillaries is that of filling the whole device from its outlet, using a high reservoir full of water and keeping the lateral inlets closed: when water starts to get out from the free end of the capillary, this is put into the tubing (already filled with the sample solution and connected to the sample reservoir) and glued. Though some water can get out of the capillary-tubing connection, making it more difficult for the glue to dry, when the glue seal has actually hardened, it holds well enough to establish flows such as those presented in Section 3.2: the water reservoir is disconnected from the outlet, the sheath flow, driven by syringe pumps, is added from the lateral inlets, and the flow velocity is varied by changing h.

This way of filling the capillary up would take too long for the 2 mm diameter capillaries, because of their greater volume. In this case, a pipette with a very thin tip (epT.I.P.S. 20 µL Microloader, Eppendorf) can be introduced into the capillary as far as it can go, and used to fill the capillary with liquid.

3.1.5 Microscopes and sample solutions

As already mentioned (Sections 3.1.2 and 3.1.3), a stereomicroscope is needed in some stages of the device fabrication. The microscope used (Olympus SZ61, Olympus GmbH, Hamburg, Germany) has been calibrated using an objective micrometer (Olympus Objective Micrometer OBM1/100): the number of pixels corresponding to a 100 µm length for the 4.5× magnification can be measured from a picture of the micrometer taken with this magnification, and is found to be 136.01 px. From this value, the scale $S(M)$ for each of the other magnifications M (ranging from .67× to 4.5×) can be retrieved simply by multiplying it by the ratio between the nominal magnification of interest and 4.5:

$$S(M) = S(4.5) \cdot \frac{M}{4.5} = \frac{136.01\,\text{px}}{100\,\mu\text{m}} \cdot \frac{M}{4.5} \tag{3.2}$$

Observing the flows into the microfluidic channel is possible thanks to a microscope capable of both bright field and fluorescence imaging (Olympus IX71, Olympus GmbH, Hamburg, Germany – equipped with a PCO.1200s camera). Bright field illumination is provided by a halogen lamp (Olympus TH4-200) placed at the top of the microscope, while fluorescence imaging works with another lamp (Olympus X-Cite 120 PC) that illuminates the sample from the bottom. Several objectives are available (see their specifics in Table 3.1): only the 10× objective and the 20× objective have been used to take the pictures displayed in the next section.

Objective	Binning	Pixel	µm	Field-of-view [µm]
2×	1	83	500	7711 × 6167
10×	1	415	500	1542 × 1234
20×	1	415	250	771 × 617
40×	1	415	125	386 × 308
60×	1	249	50	257 × 206
100×	1	415	50	154 × 123

Table 3.1: Scaling parameters for Olympus IX71 microscope.

Data acquisition can be controlled by an Open Source software, Micro-Manager [4]; the resulting images are handled using ImageJ [20].

In order to visualize the focused stream, fluorescent samples are used: either a watery 10 µM fluorescein solution, or yellow-green fluorescent beads (2 µm diameter; starting solution – from FluoSpheres® Size Kit #2, invitrogen™, Eugene, USA – contains 2% solids and is diluted with distilled water in 1 : 2000 volume ratio). The sheath flow is always distilled water. All liquids are degassed in a desiccator for at least 15 min before being employed.

3.2 Experimental results

3.2.1 Geometric features of the tested devices

We are now going to describe the dimensions of three devices that have been imaged yielding the results examined below.

The first device tested, from now on referred to as “device 1”, is made of a non-pulled, approximately 100 µm diameter capillary embedded in a central channel of nominal cross section 200 µm × 200 µm. More precise measurements of the channel side and of the capillary diameter can be seen in Figure 3.12.

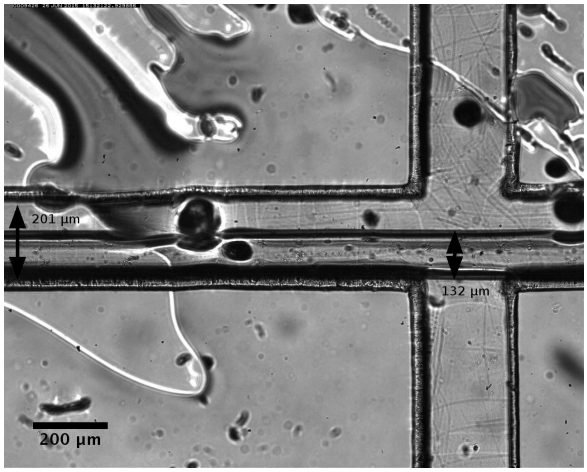

(a) *Junction between central channel and lateral inlets. The capillary is not centered. (IX*71, 10× *objective.)*

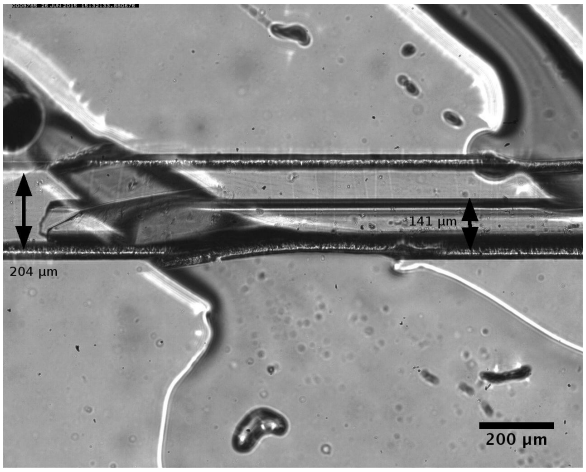

(b) *Tip of device* 1. *(IX*71, 10× *objective.)*

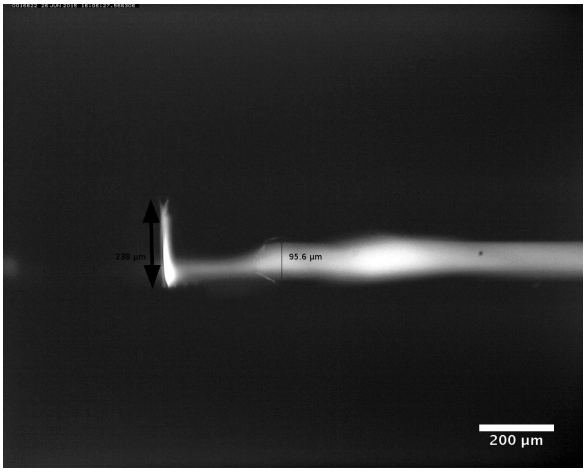

(c) *Measurement of the inner diameter of the capillary, carried out on a fluorescent image. The formation of an air bubble (eliminated before starting the actual experiment) made the fluorescein span the whole channel side, thus allowing to also measure the side of the channel. (IX*71, 10× *objective.)*

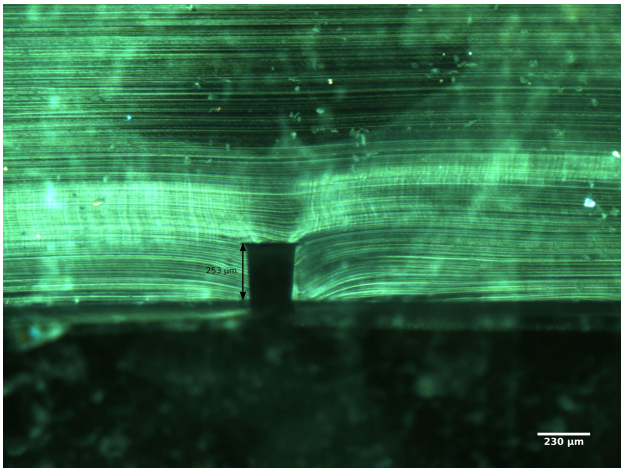

(d) *Cross section of a channel identical to the main channel of device* 1 *(obtained from the same master) and measurement of its height. (SZ*61, 4.5× *magnification.)*

Figure 3.12: Dimensions of device 1. (The weird stains on the bright field images are due to dirt on planes different from the one observed, not to fails in the structure of the channels.)

The main features of the second device tested ("device 2") can be observed in Figure 3.13: the central channel has a nominal cross section of 100 µm × 100 µm and hosts a pulled capillary. The diameter of the capillary thins down from approximately 100 µm to around 50 µm along ≈ 27 mm.

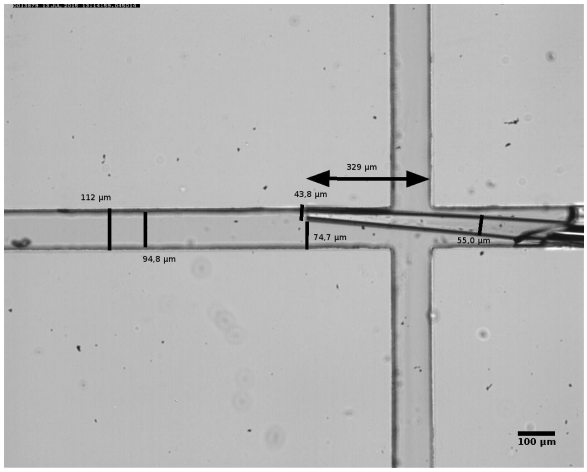

(a) *Junction between central channel and lateral inlets. The tip of the capillary is also visible, touching one wall of the channel. (IX*71*,* 10× *objective.)*

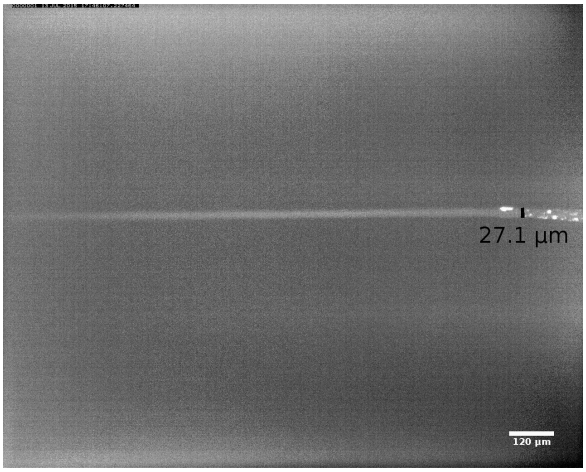

(b) *Measurement of the inner diameter of the capillary, carried out on a fluorescent image. (IX*71*,* 10× *objective.)*

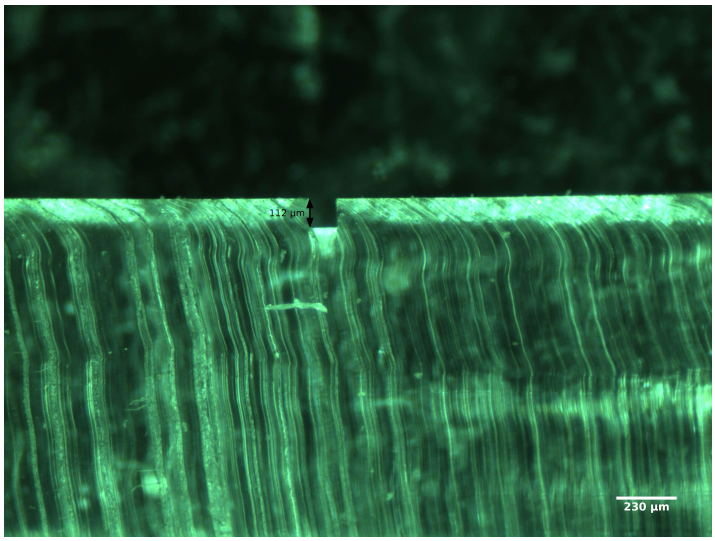

(c) *Cross section of a channel identical to the main channel of device* 2 *(obtained from the same master) and measurement of its height. (SZ*61*,* 4.5× *magnification.)*

Figure 3.13: Dimensions of device 2.

Finally, "device 3" (Figure 3.14) has again a main channel of nominal cross section of 100 µm × 100 µm. The diameter of its pulled capillary thins down from approximately 100 µm to around 16 µm in ≈ 35 mm.

As already mentioned in Section 3.1.4, the sample solution was delivered through the non-pulled capillary of device 1 by a syringe pump (so that its volume flow rate Q_{sample} was that selected using the syringe pump control software), while for the pulled capillaries of devices 2 and 3 the high reservoir method was employed. In order to know the flow rate exiting the thin tip of the capillary and entering the device, knowledge of the hydrodynamic resistance R_{hyd} of the capillary is then required: it can be retrieved from equation (1.30), given the height h of the reservoir and thus, through equation (3.1), the pressure drop Δp.

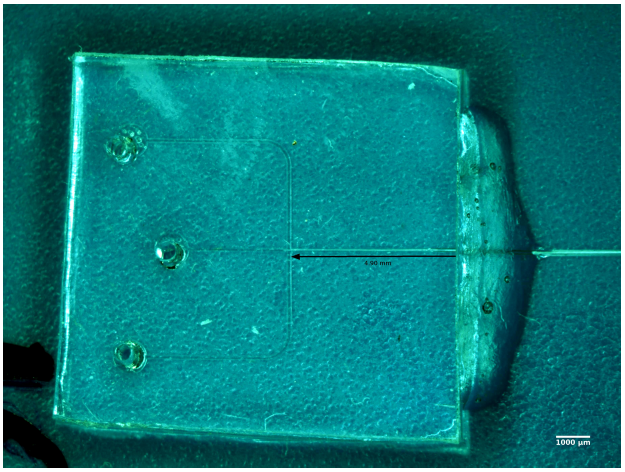

(a) *Overall view of the device. (SZ*61, .67× *magnification.)*

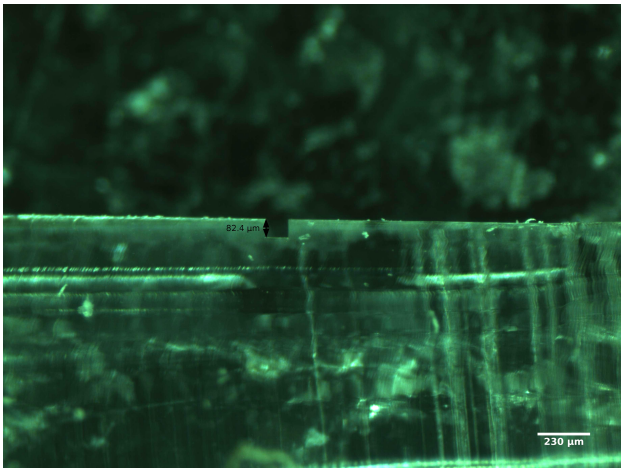

(b) *Cross section of a channel identical to the main channel of device* 3 *(obtained from the same master) and measurement of its height. (SZ*61, 4.5× *magnification.)*

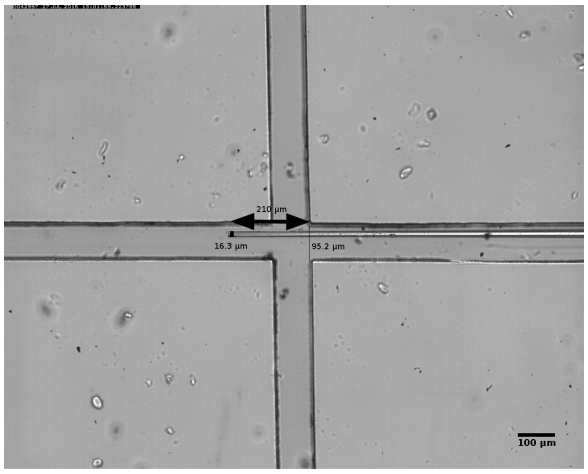

(c) *Junction between central channel and lateral inlets, and tip of the capillary. Though not centered, the capillary is not touching any wall.(IX*71, 10× *objective.)*

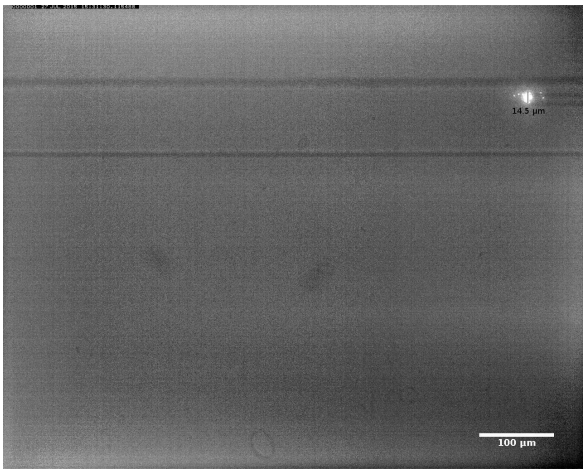

(d) *Measurement of the inner diameter of the capillary, carried out on a bright field/fluorescent image. (IX*71, 20× *objective.)*

Figure 3.14: Dimensions of device 3.

Each capillary can be seen as a series of cylindrical or trunk cone-shaped channels, depending on its form. It is convenient to ideally divide a capillary into three segments:

Segment 1 the part outside the PDMS channel, of constant diameter 100 µm;

Segment 2 the part into the channel but before the junction, approximated as a trunk cone;

Segment 3 the part from the beginning of the junction to the tip of the capillary. Because of their different shape, these parts are treated differently for the two capillaries: the one of device 2 as a trunk cone, that of device 3 as a cylinder.

The sizes of the devices, together with the hydrodynamic resistance of their capillaries (when computed), are summarized in Table 3.2.

Parameter	Device 1	Device 2	Device 3
Channel width [µm]	238 ± 2	95 ± 2	95 ± 2
Channel height [µm]	253 ± 2	112 ± 2	82 ± 2
Channel cross sectional area [µm^2]	60200 ± 700	10600 ± 400	7800 ± 300
Outer diameter, segment 1 [µm]	132 ± 2	100	100
Outer diameter, end of segment 2 [µm]	132 ± 2	55 ± 2	16 ± 2
Outer diameter, end of segment 3 [µm]	132 ± 2	42 ± 2	16 ± 2
Inner diameter, end of segment 3 [µm]	96 ± 3	27 ± 3	15 ± 1
Capillary tip cross sectional area [µm^2]	7200 ± 500	600 ± 100	170 ± 20
Length of segment 1 [cm]	–	2.5 ± 0.6	3.0 ± 0.6
Length of segment 2 [mm]	–	1.25 ± 0.01	4.90 ± 0.01
Length of segment 3 [µm]	–	329 ± 2	210 ± 2
Hydrodynamic resistance [Pa s m^{-3}]	–	$(17 \pm 2) \cdot 10^{12}$	$(5 \pm 1) \cdot 10^{14}$

Table 3.2: Geometric characterization of devices 1, 2 and 3. No error appears for the diameter of segment 1, because it has not been measured (its nominal value is taken instead). The hydrodynamic resistance of the capillary of device 1 is not needed, so it has not been computed. All errors of quantities indirectly estimated are determined by error propagation.

3.2.2 Characterization of the focused flows

A selection of bright field and fluorescence images of flows in devices 1, 2 and 3, taken using the IX71 microscope, is presented and commented below.

Device 1

A fluorescein solution was injected into the capillary of device 1 using a Hamilton Gastight #1001 syringe, and the sample flow rate was varied between 40 µL/h and 1000 µL/h. The sheath flow was delivered by two Hamilton Gastight #1005 syringes, that were always set to yield the same flow rate, ranging from 100 µL/h to 500 µL/h, so that the whole sheath flow had a volume rate $200\,\mu\text{L/h} \leq Q_{\text{sheath}} \leq 1000\,\mu\text{L/h}$ (namely, the double of that of a single syringe).

For each flow combination tried, image series were taken with the 10× objective. Image series allow us to explore the time evolution of the flow. In this case, when a single image series is examined, instabilities in the flow are revealed: the diameter of the sample flow is not constant, and throughout the series the signal can grow stronger or become fainter, sometimes even disappearing. This feature can be seen, more or less strongly, in every image series, thus it does not depend on the flow rates. An example of this phenomenon can be seen in Figure

3.15. This figure also shows the effects of the irregularities of the capillary tip (see also Figure 3.12b) on the shape of the flow.

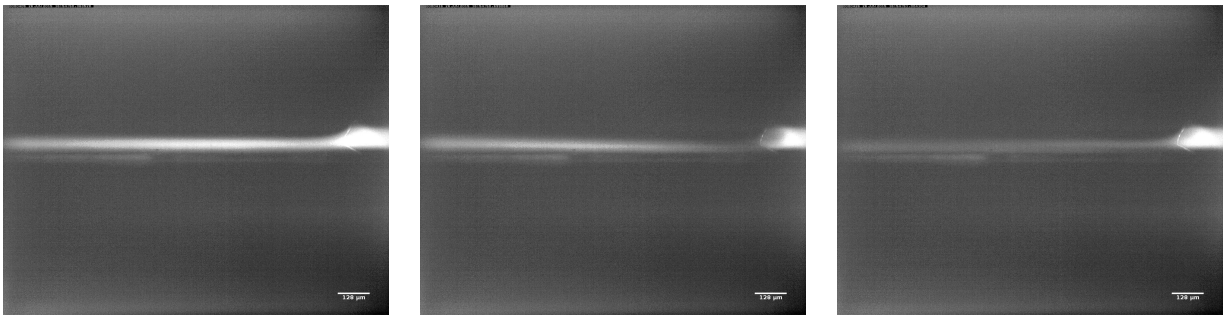

(a) *First frame:* $t = 0\,\mathrm{s}$. (b) $t = 93.2\,\mu\mathrm{s}$ (c) $t = 188\,\mu\mathrm{s}$

Figure 3.15: Instability for a sample flow rate of 100 µL/h, sheathed with a 1000 µL/h outer flow rate.

These instabilities make it difficult to define, and then measure, the width of the fluorescein flow, given the inner and outer flow rates. Nevertheless, such measurements were performed, to have a first idea of the quality of this focusing system. For each combination of sample and sheath flow rates, a frame was chosen (it was picked from the most stable segment of each image series, to be representative of the whole series). An origin for the horizontal (x-) axis was fixed as shown in Figure 3.16: ideally, the origin would be taken on the plane where the capillary ends; due to the roughness of the capillary tip, such a plane can not be defined, so the lower edge of the tip was chosen as a reference. The orientation of the x-axis is the same as that of the velocity: from the capillary (right hand side of the picture) to the PDMS channel (left hand side of the picture) .

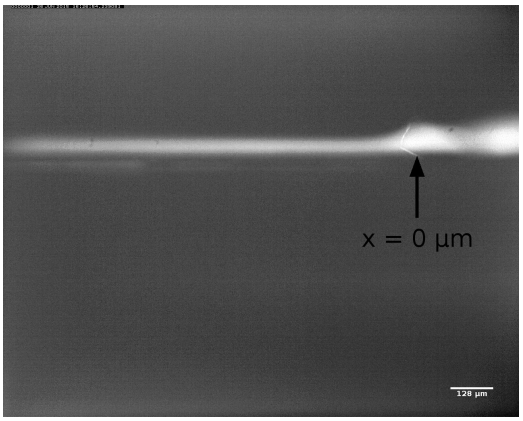

Figure 3.16: Origin point for the x-axis. Picture taken with a 40 µL/h sample flow rate and a 1000 µL/h sheath flow rate.

For each of the representative frames chosen, the width of the fluorescein flow was measured at positions $x = (0; 100; 500; 1000)$ µm. The measurements at the origin, which correspond to measurements of the capillary inner diameter, do not yield all the same value, as they ought to (see Table 3.3). The average value for the capillary inner diameter is found to be (101 ± 4) µm. For this reason, every measured width w_{meas} has been normalized, dividing it by the corresponding width at $x = 0\,\mu\mathrm{m}$ and then multiplying it by the average inner diameter, to make a comparison between different data sets possible:

$$w_{\mathrm{norm}}(x) = \frac{101\,\mu\mathrm{m}}{w_{\mathrm{meas}}(0)} w_{\mathrm{meas}}(x). \tag{3.3}$$

Sample flow rate [µL/h]	Sheath flow rate [µL/h]	Stream width at $x = 0\,\mu m$ [µm]
40	1000	98 ± 2
50	1000	100 ± 2
60	1000	101 ± 2
70	1000	96 ± 2
80	1000	101 ± 2
90	1000	108 ± 2
100	1000	100 ± 2
100	1200	101 ± 2
100	1400	100 ± 2
100	1600	101 ± 2
100	1800	95 ± 2
100	800	98 ± 2
100	200	111 ± 2
100	400	103 ± 2

Table 3.3: Capillary inner diameter for device 1.

In order to investigate the changes in the shape of the stream along the x-axis, a plot of the measured widths against the x coordinate can be made. When plotting these curves for different flow rates together 3.17, a general tendency to narrow down can be seen, but there is no definite dependence neither on the sample flow rate (3.17a) nor on the sheath flow rate (3.17b).

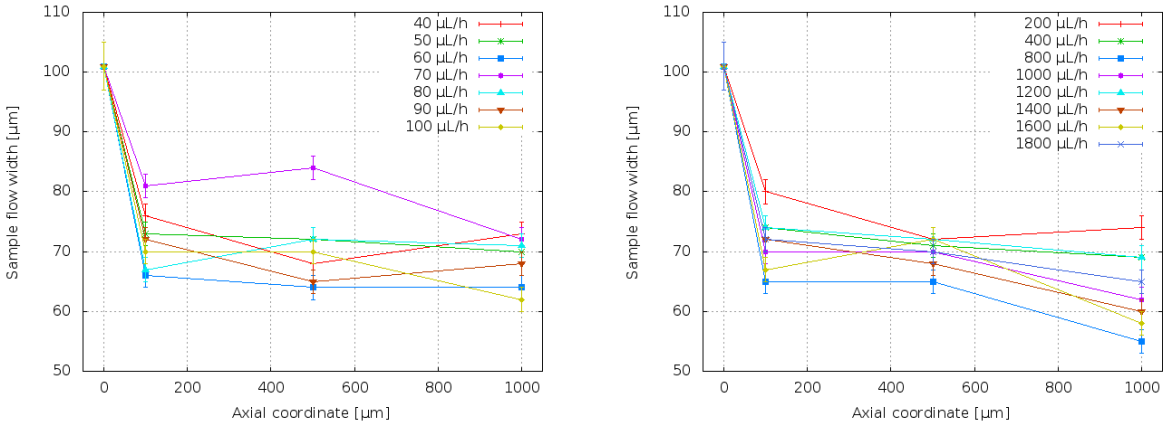

(a) *Stream profiles for different sample flow rates (the sheath flow rate is constantly* 500 µL/h*).*

(b) *Stream profiles for different sheath flow rates (the sample flow rate is constantly* 100 µL/h*).*

Figure 3.17: Stream profiles for device 1.

To better visualize this general tendency of the stream shape, we can also take the mean value of the widths for each x value, averaging over data taken at different flow rates: see Figure 3.18.

Given the small variations in width from $x = 100\,\mu m$ to $x = 1000\,\mu m$ (if compared with the rather large error bars), we may also regard the width as constant in this stretch of the x-axis: we can then consider a unique value of width for each flow rate combination, computed as the mean value of $w_{\text{norm}}(100\,\mu m)$, $w_{\text{norm}}(500\,\mu m)$ and $w_{\text{norm}}(1000\,\mu m)$. This can be used to further analyse the dependence of the width on the flow rates (or, possibly, the lack of such dependence). What we get is then Figure 3.19.

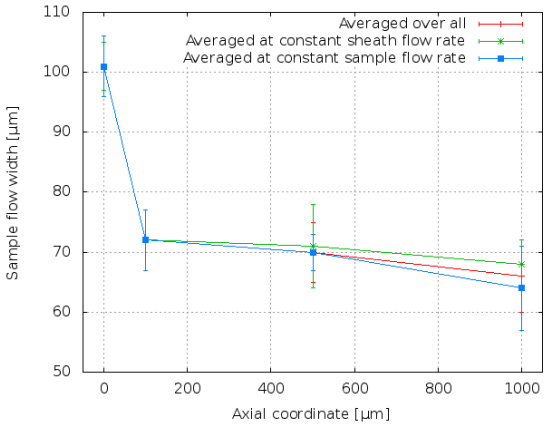

Figure 3.18: Mean stream profiles for device 1 (obtained averaging over all flow rates combinations, only on that of constant sheath flow rate or only on that of constant sample flow rate).

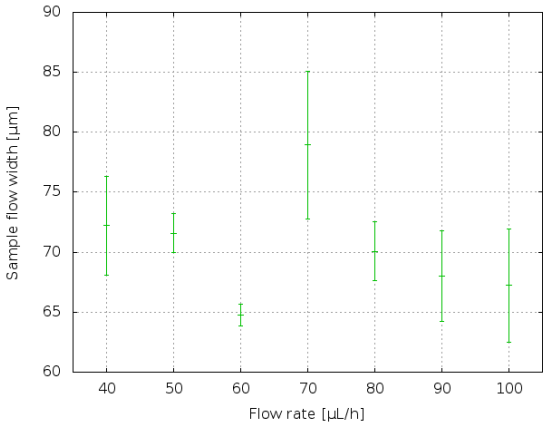

(a) *Sample stream width* versus *sample flow rate (the sheath flow rate is constantly* 500 µL/h*).*

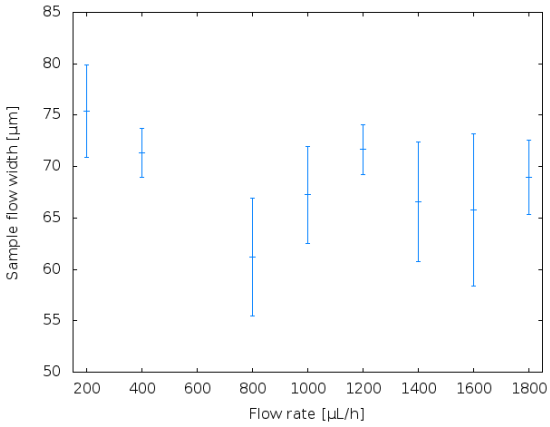

(b) *Sample stream width* versus *sheath flow rate (the sample flow rate is constantly* 100 µL/h*).*

Figure 3.19: Dependence of the width of the sample stream on flow rates.

When the sample flow rate increases at constant sheath flow rate (Figure 3.19a), an increase of the stream diameter is expected; a decrease is expected instead when the sheath flow rate grows while keeping the sample flow rate constant (Figure 3.19b). Both curves in Figure 3.19, however, resemble random distributions around a constant value, rather than variations with the flow rates. This interpretation is supported by a plot of the deviations from the mean value (Figure 3.20): the deviations are randomly distributed, as they would be for a constant distribution.

It is interesting to point out that the data acquisition has been done in the very order in which the data are presented in Table 3.3: we can then notice that two of the bigger deviations in Figure 3.20b, those of $Q_{\text{sheath}} = 800\,\mu\text{L/h}$ and $Q_{\text{sheath}} = 200\,\mu\text{L/h}$, correspond to data acquired after a "skip" in the flow rate bigger than usual, that is 1000 µL/h in the first case (the sheath flow rate was changed from 1800 µL/h to 800 µL/h) and 600 µL/h in the second case (from 800 µL/h to 200 µL/h), instead of the steps of 200 µL/h used otherwise when changing the sheath flow rate. Such big deviations from the mean value may then indicate a reaction of the system to abrupt changes of the sheath flow, though the same argument can not be used to justify the biggest deviations of Figure 3.20a.

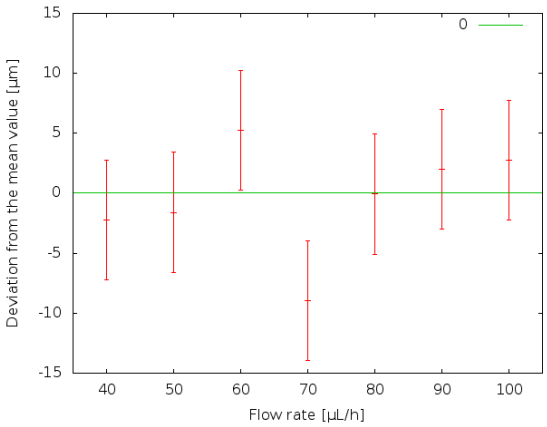

(a) *Deviations from the mean value (*(70 ± 5) µm*) for the distribution shown in Figure 3.19a.*

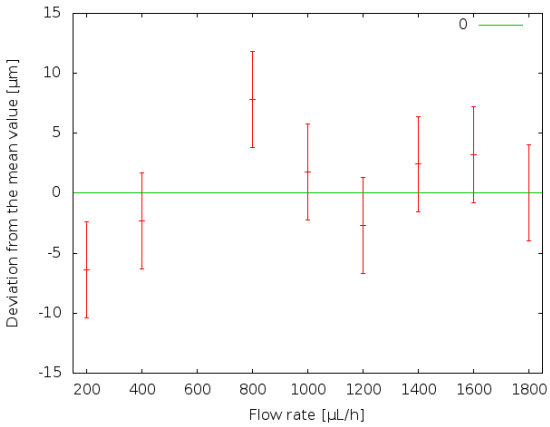

(b) *Deviations from the mean value (*(69 ± 4) µm*) for the distribution shown in Figure 3.19b.*

Figure 3.20: Deviations from the mean value for the datasets of Figure 3.19.

Device 2

In device 2, the sample flow was driven by the pressure of a liquid column. Only two different heights were used for the liquid column: $h = (6 \pm 1)$ mm and $h = (16 \pm 1)$ mm. The sheath flow was injected by two Hamilton Gastight #1005 syringes (just like for device 1), and its rate ranged from 200 µL/h to 2000 µL/h when $h = (6 \pm 1)$ mm, from 200 µL/h to 3000 µL/h when $h = (16 \pm 1)$ mm.

Using equations (1.30) (Hagen-Poiseuille law) and (3.1) (hydrostatic pressure of a column of fluid), it is possible to compute the sample flow rates corresponding to the heights of the sample column used in the experiment. Moreover, assuming that the linear velocity v_{sample} of the sample flow equals

$$v_{\text{sample}} = \frac{Q_{\text{sample}}}{S_{\text{capillary}}}, \tag{3.4}$$

with $S_{\text{capillary}}$ area of the tip of the capillary, this velocity can be estimated as well. The flow rates and linear velocities thus calculated are listed in Table 3.4.

Height [mm]	Flow rate [µL/h]	Velocity [mm/s]
(6 ± 1)	12 ± 2	6 ± 2
(16 ± 1)	33 ± 4	15 ± 4

Table 3.4: Flow rates and linear velocities of the sample flow.

The image series, taken with the 10× objective, show flows generally more stable than those observed in device 1, apart from the case of very high sheath flow rates (see Figure 3.21) or some rare event at lower sheath flow rates, probably due to the presence of an air bubble in the channel (Figure 3.22).

(a) *First frame:* $t = 0\,\mathrm{s}$. (b) $t = 0.557\,\mathrm{ms}$ (c) $t = 1.11\,\mathrm{ms}$

Figure 3.21: Instability for a sheath flow rate of 3000 µL/h; the height of the sample column is 16 mm.

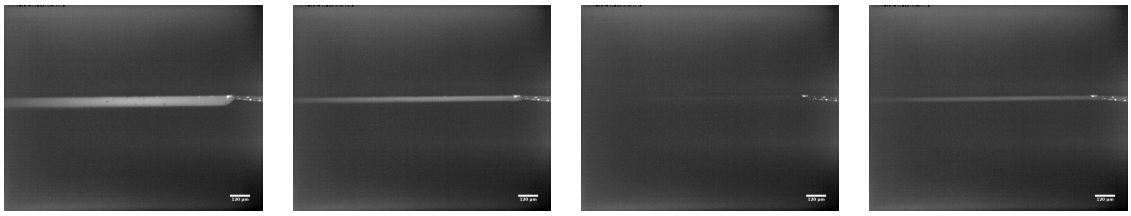

(a) *First frame:* $t = 0\,\mathrm{s}$. (b) $t = 0.557\,\mathrm{ms}$ (c) $t = 1.11\,\mathrm{ms}$ (d) $t = 1.53\,\mathrm{ms}$

Figure 3.22: Instability for a sheath flow rate of 400 µL/h; the height of the sample column is 6 mm.

The streams get thinner and thinner as the sheath flow rate grows, as can be observed even without measuring their widths, in Figure 3.23.

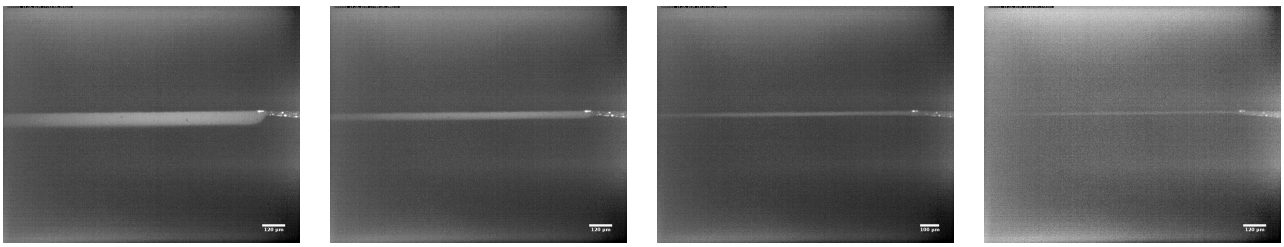

(a) $Q_{sheath} = 200\,\mu\mathrm{L/h}$. (b) $Q_{sheath} = 1000\,\mu\mathrm{L/h}$. (c) $Q_{sheath} = 2000\,\mu\mathrm{L/h}$. (d) $Q_{sheath} = 3000\,\mu\mathrm{L/h}$.

Figure 3.23: Reduction of the stream width with increasing sheath flow rates ($h = 16\,\mathrm{mm}$;).

The image series with a 6 mm high sample column and a 4000 µL/h sheath flow rate does not display any stream: such a high outer flow rate prevents the sample solution from exiting the capillary at all.

Measurements of the stream widths were performed with the same procedure as that used for device 1: after an origin for the x-axis was fixed (Figure 3.24), measurements of the width were taken at $x = (0; 100; 500; 1000)\,\mu\mathrm{m}$.

Once again, the widths at $x = 0\,\mu\mathrm{m}$ are not all the same (Table A.2, Appendix A): their mean value is $(28 \pm 2)\,\mu\mathrm{m}$ and it is used to normalize all other widths according to the following equation,

$$w_{\mathrm{norm}}(x) = \frac{28\,\mu\mathrm{m}}{w_{\mathrm{meas}}(0)} w_{\mathrm{meas}}(x). \tag{3.5}$$

This time, when plotting the width profiles along the x-axis (Figure 3.25), a dependence on the sheath flow rate emerges, which can be better understood taking an average of $w_{\mathrm{norm}}(100\,\mu\mathrm{m})$, $w_{\mathrm{norm}}(500\,\mu\mathrm{m})$ and $w_{\mathrm{norm}}(1000\,\mu\mathrm{m})$ for each sheath flow rate (Figure 3.26).

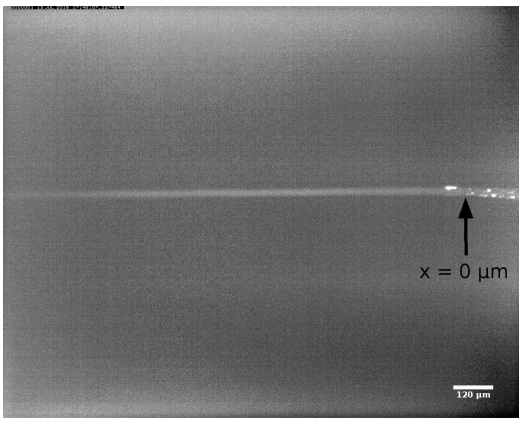

Figure 3.24: Origin point for the x-axis. Picture taken with a 6 mm high sample solution column and a 2000 µL/h sheath flow rate.

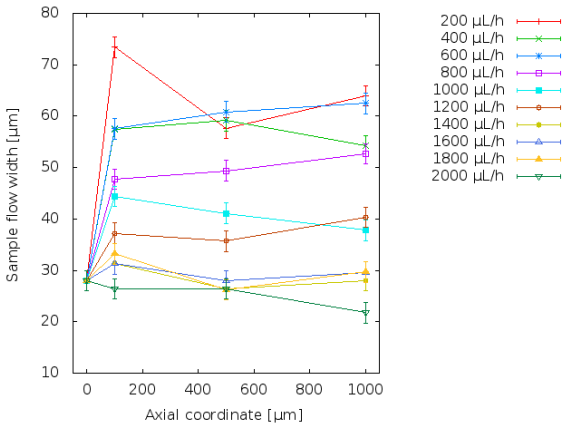

(a) *Stream profiles for different sheath flow rates ($h = 6$ mm).*

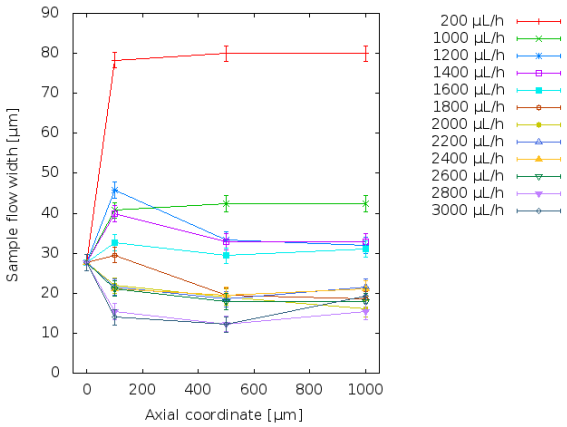

(b) *Stream profiles for different sheath flow rates ($h = 16$ mm).*

Figure 3.25: Stream profiles for device 2.

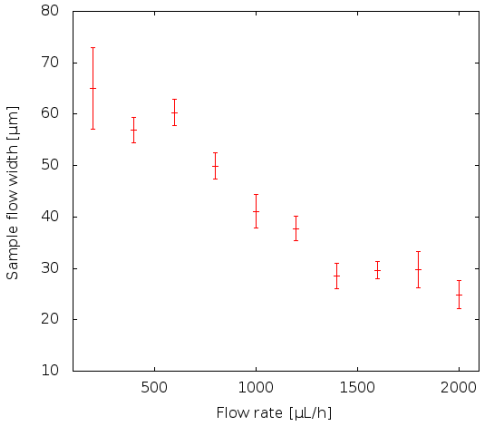

(a) *Sample stream width* versus *sheath flow rate ($h = 6$ mm).*

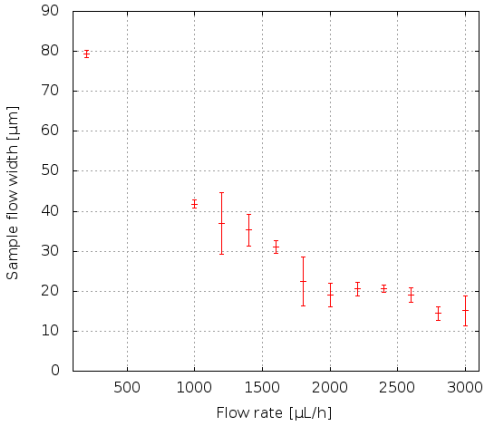

(b) *Sample stream width* versus *sheath flow rate ($h = 16$ mm).*

Figure 3.26: Dependence of the width of the sample stream on the sheath flow rate.

In fact, Figures 3.26a and 3.26b show a clear drop in the stream width as the sheath flow rate increases.

Devices 1 and 2: a comparison

In order to compare all the results obtained so far, a way to condense the information on geometry, sheath flow dynamics and sample flow dynamics is needed. As for the geometry, we can calculate the linear velocities starting from the flow rates, similarly to what already done for the sample streams of device 2: this takes into account the differences in the cross sections of the considered channels. We can then use the ratio r_{vel} of the linear velocities as a parameter to characterize the dynamics. Finally, we can have a look at the percent variation of the sample stream width $w_{\%}$, so that devices with different capillaries may be compared.

Therefore, the abscissas of Figure 3.27 were computed as:

$$r_{\text{vel}} = \frac{v_{\text{sheath}}}{v_{\text{sample}}} = \frac{Q_{\text{sheath}}}{Q_{\text{sample}}} \frac{S_{\text{capillary}}}{S_{\text{sheath}}}, \tag{3.6}$$

while its ordinates as

$$w_{\%}(x) = \frac{w_{\text{meas}}(x)}{w_{\text{meas}}(0)}. \tag{3.7}$$

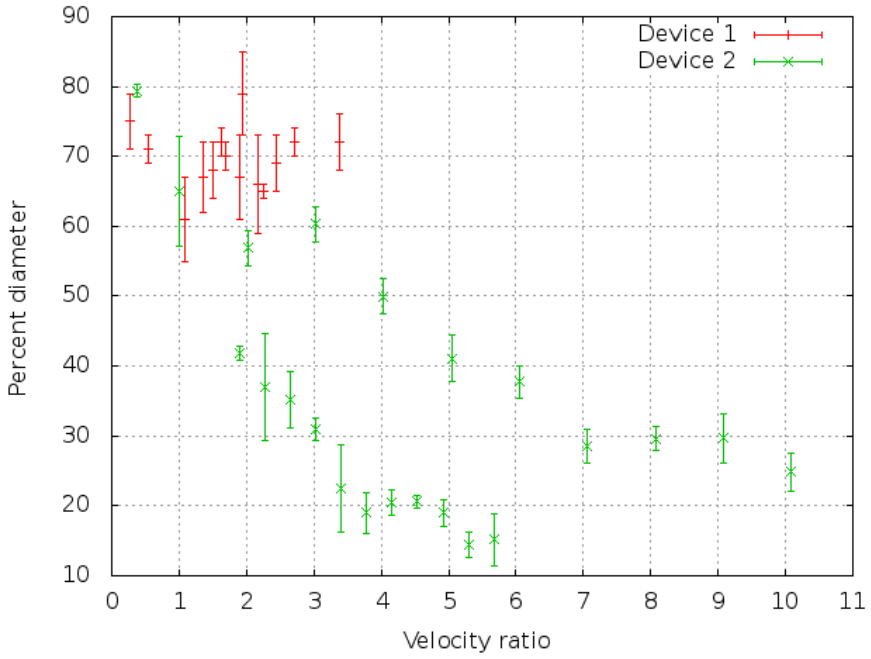

Figure 3.27: Comparison between the sample stream widths obtained with devices 1 and 2.

This plot confirms the observations made above: the focusing capabilities of device 2 are clearly appreciable, while the width of the stream in device 1 is in fact constant. Moreover, we can conclude that the velocity ratio can not uniquely qualify the dynamics of the flow even for the same device: the data points relative to device 2 form two curves (corresponding to Figure 3.26a and 3.26b respectively) instead of one.

All velocities were retrieved indirectly and their calculation is based on assumptions like the constance of the velocities on the surfaces $S_{\text{capillary}}$ and S_{sheath} and the modelling of the capillary as a series of hydrodynamic resistances hosting a creeping flow. The high relative errors committed in length measurements make the errors on the sample velocities of device 2 quite high as well: hence, we would like to have more direct measurements of them, in order to both reduce the error and confirm, or discard, the model of the capillary we have been using so far.

Device 3

More direct measurements of the sample velocities can be realized using fluorescent beads, instead of fluorescein, as our sample: the beads will leave a trace on each frame acquired, corresponding to the distance they travel during exposure (Figure 3.28).

Figure 3.28: Example of bead tracks (objective 10×; exposure time 10 ms).

Thus, knowing the exposure time t_{exp} for the single frame and measuring the length l_{tr} of the trace, the velocity v_{bead} of the bead can be recovered as

$$v_{\text{bead}} = \frac{l_{\text{tr}}}{t_{\text{exp}}}. \tag{3.8}$$

Fluorescent beads were flown through the capillary of device 3. Image series were acquired using objective 10× or 20×; the exposure time for each image was 10 ms or 20 ms. The heights of the sample column and the sheath flow rates (delivered by two Hamilton Gastight #1001 syringes) can be found in Table A.3 (Appendix A), together with the velocities measured, for each height-flow rate combination, taking an average of the values estimated using equation (3.8).

Comparing the measured velocities with those expected from our model (the same computations made to estimate the sample velocities for device 2), also listed in Table A.3, it turns out that the expected velocities are generally overestimated.

Plotting the measured velocities against the sample column height, keeping the sheath flow rate constant, it can be seen (Figure 3.29) that said velocities depend more on the sheath flow rate than on the column height.

When the same measured velocities are plotted against the sheath flow rate and at constant height, it is revealed that they increase with increasing sheath flow rates (Figure 3.30).

The linear velocities of the sheath flow look more compatible with the measured velocities of the sample flow (Table A.4, Appendix A); nevertheless, no univocal relation exists between these two quantities (different measured sample velocities correspond to the same sheath flow velocity) , nor a definite dependence can be found on the ratio between the sheath flow velocity and the sample velocity expected from the model (Figure 3.31).

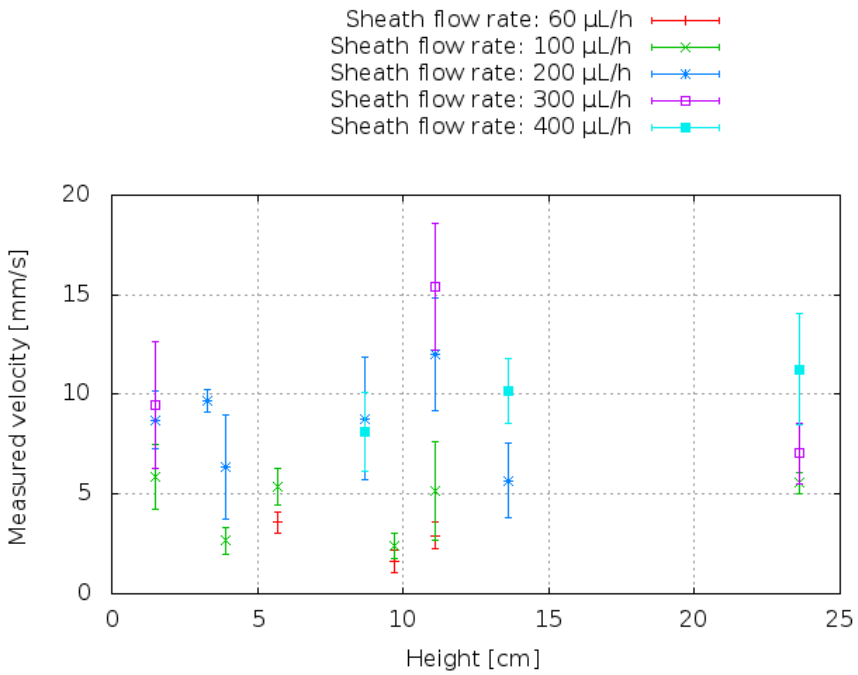

Figure 3.29: Dependence of the measured velocity on sample column heights; the different data sets are defined by their sheath flow rate; only data sets with more than two data points are shown.

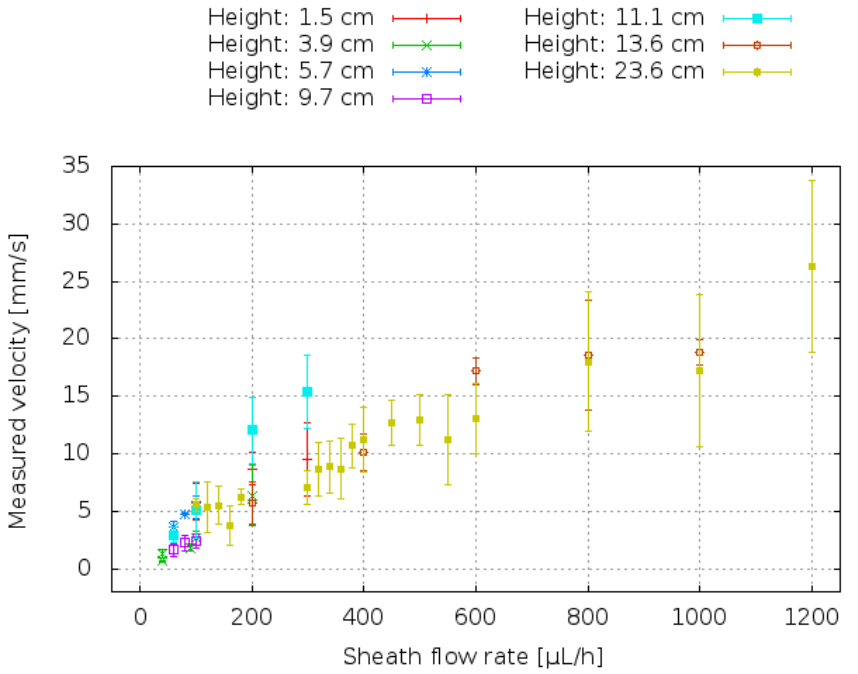

Figure 3.30: Dependence of the measured velocity on sample flow rates; the different data sets are defined by the height of the sample column; only data sets with more than two data points are shown.

These incompatibilities between model and measurements suggest that the model is not accurate enough to yield affordable predictions of the sample velocities. Anyway, during the experiments, the beads tended to clog the capillary (as in Figure 3.14d), so some of the measured velocities are lower than they would be if the capillary *lumen* were completely free.

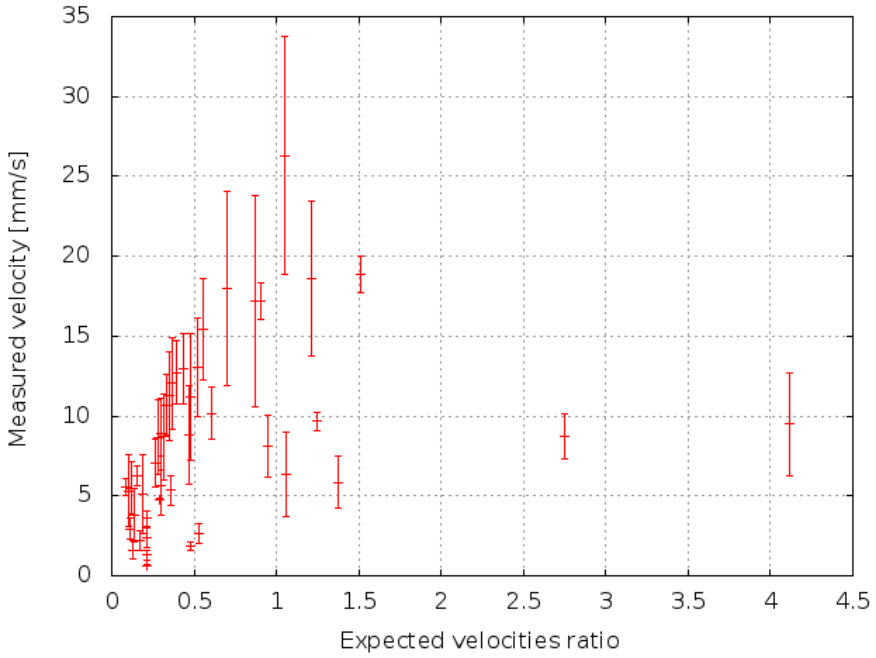

Figure 3.31: Dependence of the measured velocity on the ratio between the sheath velocity and the expected sample velocity.

3.3 Simulations and experiments: velocity comparison

As seen in Section 2.2, FEM simulations can provide information about flow velocities: we can then compare the velocities measured for device 3 with yet other previsions, made using simulations rather then equations (1.30), (3.1) and (3.4).

With this aim in mind, we performed some FEM simulations, using the geometry described in Section 2.2, but changing the radius of the sample inlet to 7.5 µm, so that the structure of device 3 could be better resembled. The input flow rates were chosen to match some of the experimental conditions: seven different sample flow rate-sheath flow rate couples were simulated, to get the velocity dependence on the sample flow rate, at constant sheath flow rate, and *vice versa*. For each simulation, the maximum velocity magnitude was retrieved as in Section 2.2, measuring the constant value that the velocity in the middle of the channel reaches for $x \gtrsim 100\,\mu m$. This maximum velocity was then converted into an expected average velocity taking the 48% of its value, in accordance with equation (2.2) and with the results of previous simulations (strictly speaking, the conversion factor 48% should not be used here, because it was determined using a slightly different geometry, the capillary radius being now 7.5 µm instead of 5 µm; nevertheless, the experimental velocity measurements are not so precise as to require a perfect reconstruction of the real geometry).

It is now possible to compare the velocity dependence on the sample flow rate and on the sheath flow rate for the velocities resulting from the experiment and from simulations.

According to the simulation results, the velocity should be constant with respect to sample flow rate variations (Figure 3.32), which can be explained noticing that the variations in sample flow rate we simulated were not particularly high. On the other hand, the measured velocities show variation, even if their order of magnitude is in accord with that of simulation. Better agreement is displayed by the dependence on sheath flow rate (Figure 3.33).

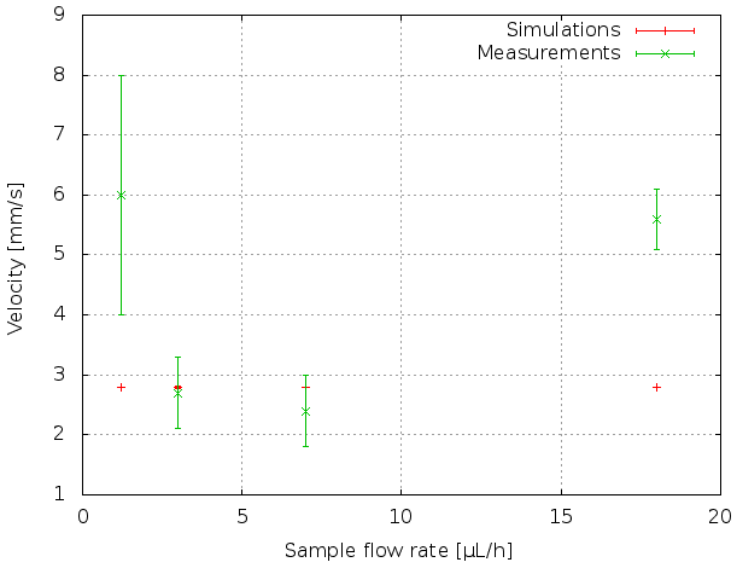

Figure 3.32: Velocity dependence on the sample flow rate ($Q_{\text{sheath}} = 100\,\mu\text{L/h}$).

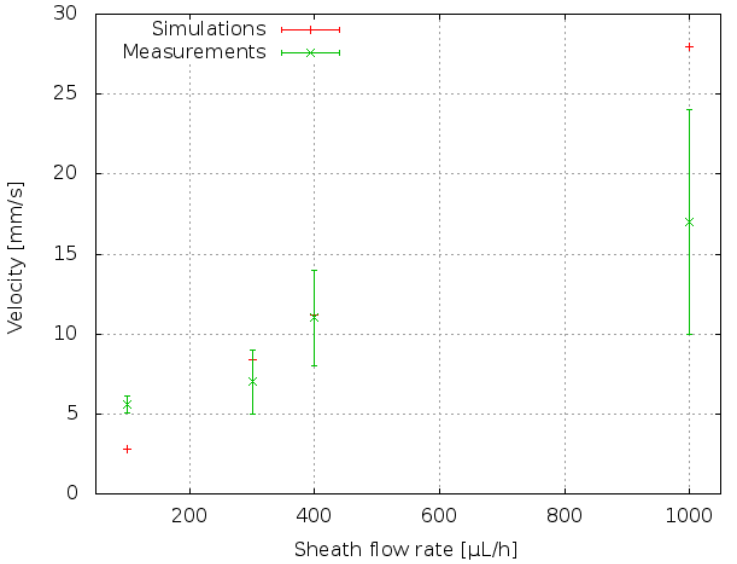

Figure 3.33: Velocity dependence on the sheath flow rate ($Q_{\text{sample}} = 18\,\mu\text{L/h}$, corresponding to $h = 23.6\,\text{cm}$).

Conclusions and outlook

The work described in these pages constitutes the foundations for the construction of a microfluidic device to be coupled with FCS microscopy in single molecule detection applications. Our approach combined state-of-the-art literature and FEM simulations to design a device capable of hydrodynamically focusing a sample flow, while controlling the velocity of the sample itself.

Basic prototypes of such a device were built and the flows they could realize were imaged and characterized, thus developing the crafting techniques needed and exploring the mathematical tools that allow to connect theoretical expectations for the system with its real features. Further simulations were carried out to point out strengths and defects of our model, in order to improve it, so that it can then be used to enhance the experimental set up in return. The building methods presented allow fast construction of disposable devices, whose reproducibility, feasible in principle, is limited by the capillary pulling step, in which the length, diameter and shape of the capillary could not be controlled strictly. A fluid delivery system was employed that enables user-controlled speeds for the flows involved; nevertheless, filling the capillary up was time consuming, because of the big dead volumes involved, and the system was very sensitive to the disturbances induced by air bubbles; moreover, the stability of the flows was limited. The "co-flow" geometry proved to be effective as a flow focusing strategy, yielding sample streams confined by a surrounding sheath flow. The small dimensions of the glass capillary used to deliver the sample flow turned out to be critical in determining the wideness of the sample stream. The theoretical estimates for flow velocities are in accord with both experiments and simulations, as far as their order of magnitude is concerned. However, there is room for improving their precision.

These outcomes encourage the prosecution of the line of action adopted so far and offer several possibilities of improvement. First of all, a better controlled crafting of the glass capillaries could enhance the device reproducibility and reduce the dead volumes; a more suitable method to cut them would also yield more regular tips and thus better streams. As for the liquid injection management, it is worth trying to use the same method for all the flows, that is to say, let the sheath solution be driven by a constant pressure, rather than a constant volume: this should yield more stable flows. Using the constant pressure of a compressed gas, such as nitrogen, instead of that of a liquid column, would widen the range of accessible pressures and make their selection more precise. Higher pressures would be advantageous because they would speed up the capillary filling, thus reducing dead times. More precise measurements of the capillary dimensions would reduce the error on hydrodynamic resistances, hence obtaining better estimates for the velocities of the sample flow: this would enable the user to choose the velocity that best fits the running experiment. A less approximate model (e.g. one that takes the parabolic profile of the velocity into account) could also work in that direction; its validity and the relevance of the resulting improvement could be tested by simulations. Once it is proven that FEM simulation results are representative of the real system, they can be used to optimize the user-controllable parameters, so that the width of the sample stream is selected at will. This optimization will then need to be tested with new experiments on improved devices.

All in all, these results constitute a good starting point for FCS-microfluidic coupling: they

both attest the factual viability of a device that can realize such a coupling and prescribe the next steps to be made to actually build it.

Acknowledgements

So many people have supported and helped me during the drawing up of this thesis, not to mention during my University studies, that I am afraid I will not be able to do them all full justice.

I can only start thanking prof. Sarah Köster for taking me into her research group and dedicating part of her time and resources to my instruction: without her, not only would this thesis never have existed, but I might also never had gone to Göttingen, thus missing the wonderful people I met there, and the great time I spent with them.

The opportunity to go to Göttingen was also provided by prof. Giampaolo Mistura, who accepted to be my internal supervisor and gave me advice on the structure and features of a master thesis.

My project was born from the collaboration between the Köster group and prof. Erwin Neher's: I was lucky enough to be assigned to this task, and the imprint of prof. Neher's remarks has been priceless.

I will find no words enough to thank Viktor Schroeder for the patience he showed in teaching me how to use the laboratory instrumentation (often repeating the same thing over and over again), in discussing with me my results (and my failures), always producing some good idea for improvement, and in reading and correcting this thesis: thank you Viktor, again and again and again.

Patience and friendliness are common features of the members of the Köster group (I wonder if they are requisites to become one!): each and every one of them contributed to this work, with suggestions, comments, explanations, good company and sympathy. So many thanks, in no particular order, to Jana, Ash, Gerrit, Johanna, Rabea, Susanne, Clément, Heidi, Tim, Christiane, Jan-Philipp, Rita, Oliva, Lotta, for sharing your knowledge and good humour and food and a piece of your lives with me.

No one can only work (not even when people at work are so great!), and the time I spent out of the lab couldn't have been better. All the merit for this goes to my friends: my new, extraordinary international friends, with whom I have been living "in a joke" for six months ("There were an Indian, a French and a Spanish going to a party, when..."). Thanks to Carla, who, mind you, is Catalan, not Spanish; thanks to – uuuuuoooooooooooooo! – Cristina; thanks to Luca, truly one of us; thanks to a very creepy Karthik; thanks to the overworked Enikő (please get some rest!); thanks to Gabriella, for feeding us all; thanks to Philipp and his "German dance"; thanks to the slackline-addicted Clément; thanks to Laureen for being a non-beer-drinking German; thanks to Katja for the brief but wonderful time spent together. I have been so incredibly lucky to meet you!

And my old friends, though far, have been as close as they could be: here, even if I know they would perfectly understand English, I feel compelled to switch to Italian. Grazie Sofi e Nico, per la vostra assidua presenza e le vostre doti canore, state accumulando un tesoro in biscotti, nell'alto dei Cieli.

E tornando in Italia, non posso non pensare a chi ha accompagnato la mia vita patavina: grazie alle migliori conquiline (o dovrei dire ex-coinquiline? tristezza...) di sempre, la Ire, la Eli, la Laura (le mie "mamme" che mi pedinavano quando andavo in palestra...), la Fra e la

Carola, che di diritto si guadagnano un affettuoso articolo davanti al nome (e non me ne voglia troppo la grammatica). Grazie a quegli amici impareggiabili che sono stati la Fra (un'altra!) e la Cami (a quando il prossimo sushi?), Ionuț e Gianluca (al mio fianco nella strenua lotta contro i preamplificatori), Giorgio e Veronica (continuo a domandarmi come possa la seconda sopportare il primo...).

Grazie a Stefano, che mi è stato vicino negli ultimi sei mesi, oltre che nei quattro anni precedenti... ma forse qui dovrei soprattutto ringraziare l'Erasmus, per aver fatto scoprire a Stefano lo strabiliante utilizzo del telefono e di Skype per comunicare con le persone lontane – speriamo che non se ne dimentichi.

Mille grazie anche alla mia famiglia, nonne zie zii cugine e cugini, che non so come riescono a coccolarmi e viziarmi anche da lontano (ma questo lo sapevo già da tanto tempo). Un milione di miliardi di grazie alla Lisa, alla mamma e al babbo, la lista di motivi è interminabile, la mia gratitudine inesprimibile, il mio affetto infinito.

Appendix A

Tables

Some additional data, mentioned in Sections 2.2 and 3.2.2, are presented in the tables below.

Q_{sample} [µL/h]	Q_{sheath} [µL/h]	Expected v_{sample} [m/s]	Expected v_{sheath} [m/s]	r_{vel}
[illegible]	[illegible]	[illegible]	[illegible]	[illegible]

Table A.1: Flow rates used as inputs for the FEM simulations performed, and correspondent sample and sheath flow linear velocities.

Sample column height [mm]	Sheath flow rate [µL/h]	Stream width at $x = 0\,\mu\text{m}$ [µm]
[illegible]	[illegible]	[illegible]

Table A.2: Capillary inner diameter for device 2.

h [cm]	Q_{sheath} [µL/h]	Expected velocity [mm s^{-1}]	Measured velocity [mm s^{-1}]
[illegible]	[illegible]	[illegible]	[illegible]

Table A.3: Measured velocities. They are obtained averaging a different number of data points (from only 2 to 26), depending on the number of tracks visible in the images acquired.

h [cm]	Q_{sheath} [µL/h]	Sheath velocity [mm s^{-1}]	Measured velocity [mm s^{-1}]
[illegible]	[illegible]	[illegible]	[illegible]

Table A.4: Measured velocities. They are obtained averaging a different number of data points (from only 2 to 26), depending on the number of tracks visible in the images acquired.

Bibliography

[1] Thomas Dertinger et al. "Fast, background-free, 3D super-resolution optical fluctuation imaging (SOFI)". In: *Proceedings of the National Academy of Sciences* (2009).

[2] Petra S. Dittrich and Andreas Manz. "Single-molecule fluorescence detection in microfluidic channels – the Holy Grail in μTAS?" In: *Analytical and bioanalytical chemistry* (2005).

[3] Chaoqing Dong and Jicun Ren. "Coupling of fluorescence correlation spectroscopy with capillary and microchannel analytical systems and its applications". In: *Electrophoresis* (2014).

[4] Arthur Edelstein et al. "Computer Control of Microscopes Using μManager". In: *Current Protocols in Molecular Biology* (2010).

[5] Carlo S. Effenhauser et al. "Integrated Capillary Electrophoresis on Flexible Silicone Microdevices: Analysis of DNA Restriction Fragments and Detection of Single DNA Molecules on Microchips". In: *Analytical Chemistry* (1997).

[6] Elliot L. Elson. "Fluorescence Correlation Spectroscopy: Past, Present, Future". In: *Biophysical Journal* (2011).

[7] Elliot L. Elson and Douglas Magde. "Fluorescence Correlation Spectroscopy. I. Conceptual Basis and Theory". In: *Biopolymers* (1974).

[8] *Finite Element Method*. Wiley, 2012.

[9] *Fluid Mechanics*. Elsevier, 2012.

[10] Peter B. Howell Jr et al. "Two simple and rugged designs for creating microfluidic sheath flow". In: *Lab on a Chip* (2008).

[11] Wonje Jeong et al. "Hydrodynamic microfabrication *via* "on the fly" photopolymerization of microscale fibers and tubes". In: *Lab on a Chip* (2004).

[12] Douglas Magde, Elliot Elson, and W. W. Webb. "Thermodynamic Fluctuations in a Reacting System – Measurement by Fluorescence Correlation Spectroscopy". In: *Physical Review Letters* (1972).

[13] Douglas Magde, Watt W. Webb, and Elliot L. Elson. "Fluorescence Correlation Spectroscopy. III. Uniform Translation and Laminar Flow". In: *Biopolymers* (1978).

[14] Xiaole Mao, John R. Waldeisen, and Tony J. Huang. ""Microfluidic drifting" – implementing three-dimensional hydrodynamic focusing with a single-layer planar microfluidic device". In: *Lab on a Chip* (2007).

[15] Barry R. Masters. "The Development of Fluorescence Microscopy". In: *Encyclopedia of Life Sciences* (2010).

[16] J. Cooper McDonald et al. "Fabrication of microfluidic systems in poly(dimethylsiloxane)". In: *Electrophoresis* (2000).

[17] Doogie Oh et al. “Development of Time-Integrated Multipoint Moment Analysis for Spatially Resolved Fluctuation Spectroscopy with High Time Resolution”. In: *Biophysical Journal* (2011).

[18] Lars Onsager. “Reciprocal relations in irreversible processes. I”. In: *Physical Review* (1931).

[19] Suzette A. Pabit and Stephen J. Hagen. “Laminar-Flow Fluid Mixer for Fast Fluorescence Kinetics Studies”. In: *Biophysical Journal* (2002).

[20] Caroline A. Schneider, Wayne S. Rasband, and Kevin W. Eliceiri. “NIH Image to ImageJ: 25 years of image analysis”. In: *Nature Methods* (2012).

[21] Olivier J.A. Schueller et al. “Reconfigurable diffraction gratings based on elastomeric microfluidic devices”. In: *Sensors and Actuators* (1998).

[22] Rhutesh K. Shah et al. “Designer emulsions using microfluidics”. In: *Materials Today* (2008).

[23] Claire Simonnet and Alex Groisman. “Two-dimensional hydrodynamic focusing in a simple microfluidic device”. In: *Applied Physics Letters* (2005).

[24] Narayan Sundararajan et al. “Three-Dimensional Hydrodynamic Focusing in Polydimethylsiloxane (PDMS) Microchannels”. In: *Journal of microelectromechanical Systems* (2004).

[25] Abel L. Thangawng et al. “A simple sheath-flow microfluidic device for micro/nanomanufacturing: fabrication of hydrodynamically shaped polymer fibers”. In: *Lab on a Chip* (2009).

[26] *Theoretical Microfluidics*. Oxford University Press, 2008.

[27] Tuan M. Tran, Sean Cater, and Adam R. Abate. “Coaxial flow focusing in poly(dimethylsiloxane) microfluidic devices”. In: *Biomicrofluidics* (2014).

[28] Nicholas Watkins et al. “A robust electrical microcytomer with 3-dimensional hydrofocusing”. In: *Lab on a Chip* (2009).

[29] Guisheng Zhuang, Thomas G. Jensen, and Jörg P. Kutter. “Detection of unlabeled particles in the low mictrometer size range using light scattering and hydrodynamic 3D focusing in a microfluidic system”. In: *Electrophoresis* (2012).